

**O. Soupiona, S. Samaras, P. Ortiz-Amezcuca, C. Böckmann, A.
2 Papayannis, G.A. Moreira, J.A. Benavent-Oltra, J.L. Guerrero-
Rascado, A.E. Bedoya-Velásquez, F.J. Olmo, R. Román, P. Kokkalis, M.
4 Mylonaki, L. Alados-Arboledas, C.A. Papanikolaou, R. Foskinis,**
**Retrieval of optical and microphysical properties of transported
6 Saharan dust over Athens and Granada based on multi-wavelength
Raman lidar measurements: Study of the mixing processes,**
8 Atmospheric Environment,
2019,
10 116824,
ISSN 1352-2310,
12 <https://doi.org/10.1016/j.atmosenv.2019.116824>.

14 Retrieval of optical and microphysical properties of transported Saharan dust
15 over Athens and Granada based on multi-wavelength Raman Lidar
16 measurements: study of the mixing processes

16 O. Soupiona^{1*}, S. Samaras^{2,5}, P. Ortiz-Amezcu^{3,4}, C. Böckmann⁵, A. Papayannis¹, G.A.
17 Moreira^{3,4,6}, J.A. Benavent-Oltra^{3,4}, J.L. Guerrero-Rascado^{3,4}, A.E. Bedoya-Velásquez^{3,4,7},
18 F.J. Olmo^{3,4}, R. Román^{3,4,8}, P. Kokkalis⁹, M. Mylonaki¹, L. Alados-Arboledas^{3,4}, C.A.,
19 Papanikolaou¹, R. Foskinis¹

20 ¹Laser Remote Sensing Unit, Physics Department, School of Applied Mathematics and Physical Sciences,
21 National Technical University of Athens, 15780 Zografou, Greece

22 ²German Aerospace Center (DLR), German Remote Sensing Datacenter (DFD), Wessling, Germany

23 ³Andalusian Institute for Earth System Research (IISTA-CEAMA), 18006, Granada, Spain

24 ⁴Department of Applied Physics, University of Granada, 18071, Granada, Spain

25 ⁵Institute of Mathematics, Potsdam University, 14469 Potsdam, Germany

26 ⁶Institute of Research and Nuclear Energy (IPEN), São Paulo, Brazil

27 ⁷Sciences Faculty, Department of Physics, Universidad Nacional de Colombia, Medellín, Colombia

28 ⁸Grupo de Óptica Atmosférica (GOA), Universidad de Valladolid, Paseo Belén, 7, 47011, Valladolid, Spain

29 ⁹Department of Physics, Kuwait University, P.O. Box 5969, Safat 13060, Kuwait

30
31
32 *Correspondence to: O. Soupiona (soupiona.rania@gmail.com)

33
34 **Abstract**

35 In this paper we extract the aerosol microphysical properties for a collection of mineral dust cases
36 measured by multi-wavelength depolarization Raman lidar systems located at the National
37 Technical University of Athens (NTUA, Athens, Greece) and the Andalusian Institute for Earth
38 System Research (IISTA-CEAMA, Granada, Spain). The lidar-based retrievals were carried out
39 with the Spheroidal Inversion eXperiments software tool (SphInX) developed at the University of
40 Potsdam (Germany). The software uses regularized inversion of a two-dimensional enhancement
41 of the Mie model based on the spheroid-particle approximation with the aspect ratio determining
42 the particle shape. The selection of the cases was based on the transport time from the source
43 regions to the measuring sites. The aerosol optical depth as measured by AERONET ranged from
44 0.27 to 0.54 (at 500 nm) depending on the intensity of each event. Our analysis showed the hourly
45 mean particle linear depolarization ratio and particle lidar ratio values at 532 nm ranging from 11
46 to 34% and from 42 to 79 sr respectively, depending on the mixing status, the corresponding air
47 mass pathways and their transport time. Cases with shorter transport time showed good agreement
48 in terms of the optical and SphInX-retrieved microphysical properties between Athens and Granada
49 providing a complex refractive index value equal to $1.4+0.004i$. On the other hand, the results for
50 cases with higher transport time deviated from the aforementioned ones as well as from each other,
51 providing, in particular, an imaginary part of the refractive index ranging from 0.002 to 0.005.
52 Reconstructions of two-dimensional shape-size distributions for each selected layer showed that
53 the dominant effective particle shape was prolate with diverse spherical contributions. The retrieved
54 volume concentrations reflect overall the intensity of the episodes.

55
56 **Introduction**

58 Mineral dust particles have a great impact on the Earth's radiation budget, directly by scattering
60 and absorbing the solar and terrestrial (thermal) radiation and indirectly by acting as cloud
62 condensation nuclei (CCN) and/or ice nuclei (IN), thus, influencing clouds' optical and
64 microphysical properties as well as their lifetimes (Forster et al., 2007; Atkinson, et al., 2013; IPCC,
66 2013; Mamouri & Ansmann, 2015; Seinfeld et al., 2016; Karydis et al., 2017). The Saharan desert
68 is considered as the Earth's largest source of mineral dust (Prospero et al., 2002; Washington et al.,
2003). In the regions neighboring this desert, the presence of mineral dust reveals air transport due
to favorable environmental conditions for cyclone activity of the air masses (Prospero, 1996;
Dunion and Velden, 2004; Gkikas et al., 2015). However, desert dust in most of the cases is not
just a mixture of mineral components, but of other components too. This is because anthropogenic
and marine air masses mainly from local and long-range pollution are frequently mixed to air
masses dominated by mineral dust (Kallos, 1998; Valenzuela et al., 2014).

70 Dust transport events over the Mediterranean region are usually observed over southern Europe
due to cyclone winds (Escudero et al., 2005; Kallos et al., 2006; Guerrero-Rascado et al., 2008;
72 Schepanski and Knippertz, 2011; Fiedler et al., 2014; Flaounas et al., 2015) and seem to have an
increasing trend over the last decades (Ganor et al., 2010; Knippertz and Todd, 2012). There is a
74 clear difference between Eastern and Western Mediterranean dust outbreaks as was pointed out in
previous studies (Ganor et al., 2010; Gkikas et al., 2009). In the Western Mediterranean the African
76 dust occurrence is higher in summer (Salvador et al., 2014), while conventional meteorological
mechanisms (low pressure systems) provoke a rapid transport of dust towards the Eastern
78 Mediterranean, usually from spring to autumn (Papayannis et al., 2008). More specifically, these
three seasons of increased atmospheric dust are summarized in March–May, June–August and
80 September–October as shown by Papayannis et al. (2008) and Soupiona et al. (2018).

Research focusing on the aerosol optical and microphysical properties is needed since these
82 properties change rapidly in processes of aging and mixing (e.g. coagulation, humidification,
scavenging by precipitation, particle phase conversion). Due to the diversity of these processes and
84 the different aging degrees, there are still large uncertainties in aerosol microphysical properties.
For this purpose, long-term measurements and analyses have been performed in previous years
86 (Balis et al., 2004; Amiridis et al., 2005; Papayannis et al., 2005; Lyamani et al., 2005, 2006a,b,
2008; Mona et al., 2006; Pérez et al., 2006; Papayannis et al., 2008; Preißler et al., 2013; Soupiona
88 et al., 2018).

Light detection and ranging (lidar) instruments are among the most powerful and suitable tools for
90 retrieving vertically the aerosol optical properties with high temporal and spatial resolution (Balis
et al., 2006; Mattis et al., 2008; Mona et al., 2012; Zuev et al., 2017). The particle extinction (α_{aer})
92 and backscatter coefficients (β_{aer}) and its derived products [lidar ratio (LR), backscatter-related and
extinction-related Ångström exponent (AE_{β} and AE_{α}), ratio of lidar ratios (LR532/LR355)] in
94 various wavelengths are commonly used for aerosol typing (Müller et al., 2007; Groß et al., 2011;
Burton et al., 2012; Groß S., 2013; ; Nicolae et al., 2013; Burton et al., 2015; Groß et al., 2015) as
96 they are related to particle size and composition. The lidar depolarization technique (Sassen, 2005)
is also used for aerosol typing, since it provides information about the non-sphericity of the studied
98 particles. Moreover, Böckmann and Osterloh (2014), based on simulations, showed that
depolarization measurements play a crucial role for the derivation of the microphysical properties
100 of irregularly-shaped particles, like mineral dust. The retrieval of these microphysical properties
is possible by using combined optical data-sets as inputs in mathematical inversion codes based on
102 regularization of the resulting ill-posed problem (see e.g. Böckmann et al., 2005; Samaras et al.,
2015; Veselovskii et al., 2016; Müller et al., 2016).

104 In this study we show the great potential of lidar stand-alone retrievals of non-spherical aerosol
microphysical properties. The main aim of this work is to present the aerosol optical and
106 microphysical properties during selected Saharan dust events over Athens (Greece; NE

108 Mediterranean) and Granada (Spain; NW Mediterranean) focusing on short range to long range
110 dust processes. We selected specific dust transport cases that were interesting in our records
112 regarding their transport time and mixing process whose datasets allowed for stable microphysical
114 inversions. A general description of the instrumentation used is given in Section 2, while section 3
gives a brief description of the Spheroidal Inversion eXperiments (SphInX) software tool. Section
4 describes the criteria for the selection and air mass classification of the four dust cases presented.
Section 5 is mainly devoted to the results of the mineral dust optical and microphysical properties
retrieved over the two aforementioned stations. Section 6 summarizes this work.

1. Measurement Sites and Instrumentation

116 Athens and Granada stations are included in the network of i) EARLINET (since 2000 and 2004
118 respectively) in compliance with the network's quality assurance criteria and standards, both at
the hardware and software levels (Böckmann et al., 2004; Matthais et al., 2004; Freudenthaler,
2008; Pappalardo et al., 2014) and ii) AERONET (since 2008 and 2002 respectively). For nighttime
120 measurements, used in this study from both stations, the Raman technique is applied as proposed
by Papayannis et al. (1990) and Ansmann et al. (1992) to retrieve the α_{aer} and β_{aer} vertical profiles,
122 with systematic uncertainties of ~5–15% and ~10–25% respectively (Ansmann et al., 1992; Mattis
et al., 2002). Therefore, the corresponding systematic uncertainty of the retrieved lidar ratio values
124 is of order ~11–30%, while the mean uncertainty for AE_{α} and AE_{β} is of order 7–21% and 14–35%
respectively (Kokkalis, 2012).

1.1. Athens Raman lidar depolarization system (EOLE)

126 The multiwavelength Raman lidar system EOLE (aErosol and Ozone Lidar systEm) of the National
128 Technical University of Athens (NTUA, 37.97° N, 23.79° E, elev. 212 m a.s.l.) is located at the
Laser Remote Sensing Unit (LRSU) of NTUA. Its emission unit is based on a Nd:YAG laser,
130 emitting high energy laser pulses at 355, 532 and 1064 nm with a repetition rate of 10 Hz. Its spatial
and temporal resolution is 7.5 m and 100 s respectively. The receiving unit, based on a Cassegrainian
132 telescope of 300 mm and dichroic mirrors, is able to detect and discriminate the elastic
backscattered lidar signals at 355, 532 and 1064 nm and the Raman backscattered ones at 387, 607
134 and 407 nm. The geometrical specification of EOLE makes feasible the full overlap of the laser
beam with the receiver field of view to be reached at heights of the order of 800 m a.g.l. (Kokkalis,
136 et al., 2012; Kokkalis, 2017). An additional depolarization channel at 355 nm was added in 2016
in order to obtain the linear particle and volume depolarization ratio vertical profiles in the
138 atmosphere. For its calibration the $\pm 45^\circ$ calibration method is implemented (Freudenthaler et al.,
2009).

1.2. Granada Raman lidar depolarization system (MULHACEN)

140 The multiwavelength Raman lidar system MULHACEN (LR331D400 from Raymetrics S.A.),
142 located at the Andalusian Institute for Earth System Research (IISTA-CEAMA) of Granada (37.16°
N, 3.61°W, elev. 680 m asl), is configured in a monostatic biaxial alignment pointing vertically to
144 the zenith (Guerrero Rascado et al., 2008; 2009). A pulsed Nd:YAG laser with emission at
wavelengths of 355, 532 and 1064 nm is used as a radiation source. The spatial resolution is 7.5 m
146 and the temporal resolution 1 min. The backscattered signals are collected by a Cassegrainian
telescope and split by dichroic mirrors to detect elastic signals at 355, 532 (in parallel and
148 perpendicular polarizations) and 1064 nm and Raman shifted signals at 387, 607 and 408 nm. Due
to the instrument setup, the incomplete overlap limits the lowest possible detection height at 500 m
150 a.g.l. (around 1200 m a.s.l.) (Guerrero-Rascado et al., 2010; Navas-Guzmán et al., 2011). The lidar
system was upgraded in 2010 to enable the application of the $\pm 45^\circ$ calibration method as presented
152 in Bravo-Aranda et al. (2013).

1.3. CIMEL Sun-sky radiometers

154 The columnar aerosol optical and microphysical properties used in this work are provided by
 155 AERONET network (<http://aeronet.gsfc.nasa.gov>, Holben et al., 1998) which uses Sun/sky
 156 photometers (CIMEL). These instruments perform automatic measurements of the direct solar
 158 irradiance at wavelengths of 340, 380, 440, 500, 675, 870, 940 and 1020 nm and diffuse sky
 160 radiance at 440, 675, 870 and 1020 nm, respectively. The uncertainty of the aerosol size distribution
 retrieved by the sky radiance measurements is based on the calibration uncertainty of each
 wavelength, assumed to be $< \pm 5\%$. More details can be found in Dubovik and King (2000) and
 Dubovik et al. (2006).

162 Due to strict criteria imposed by the AERONET inversion algorithm and the reduced sampling of
 almucantar sky radiance measurements, there were very few level 2.0 inversion retrievals for both
 164 Athens and Granada. Thus, the AERONET level 1.5 data (cloud screened data with pre- and post-
 calibrations applied) of Version 3 was used providing information regarding the columnar aerosol
 166 optical depth (AOD) at 500 nm, AE and Fine Mode fraction (FMF), the particle volume size
 distribution (with particle radius range from 0.05 to 15 μm), the single scattering albedo (SSA) and
 168 the complex refractive index (CRI). The analysis of these columnar properties for Athens and
 Granada provides information about how the dust layers affect the atmospheric features at each
 170 site.

2. SphInX algorithm

172 The Spheroidal Inversion eXperiments (SphInX) software tool has been developed at the
 University of Potsdam (Samaras, 2016) within the Initial Training for atmospheric Remote Sensing
 174 (ITaRS) project (2012-2016). This software provides an automated process to carry out
 microphysical retrievals from synthetic and real lidar data inputs and further to evaluate statistically
 176 the inversion outcomes. SphInX software was created to handle non-spherical particles using a two-
 dimensional (2D) generalization of the Mie model and considering the spheroid-particle
 178 approximation. A spheroid is geometrically obtained from a revolution of an ellipse about one of
 its principle axes. Denoting the semi-minor axis with n and the semi-major axis with b , the aspect
 180 ratio ($a = n/b$) can characterize three possible particle shapes: oblate ($a < 1$), sphere ($a = 1$),
 prolate ($a > 1$). Particle distributions are the main products of the regularized inversion but here
 182 depend not only on size (r) but also on shape (α), which is the reason they are referred to as shape-
 size distributions. There are several common microphysical parameters (redefined to suit the
 184 advanced model) and other new shape parameters introduced in SphInX, which can be calculated
 by knowing the volume shape-size distribution. For this study we will restrict to the following
 186 parameters:

- the total volume concentration: $u_t = \int_{a_{min}}^{a_{max}} \int_{r_{min}}^{r_{max}} u(r, a) dr da$ $[\mu\text{m}^3\text{cm}^{-3}]$ (1)

- the surface-area concentration $a_t = \int_{a_{min}}^{a_{max}} \int_{r_{min}}^{r_{max}} \frac{3}{\pi r^3} G(r, a) u(r, a) dr da$ $[\mu\text{m}^2\text{cm}^{-3}]$ (2)

190 , where the function $G(r, a)$ denotes the spheroidal geometrical cross section of the particle, which
 can be explicitly computed as follows:

$$G(r, a) = \begin{cases} 2\pi \left[n^2 + \frac{b^2}{e} \tanh^{-1}(e) \right], & \text{where } e = \sqrt{1 - b^2/n^2}, \text{ if } a < 1, \\ 4\pi r^2, & \text{if } a = 1, \\ 2\pi \left[n^2 + \frac{nb}{e} \sinh^{-1}(e) \right], & \text{where } e = \sqrt{1 - n^2/b^2}, \text{ if } a > 1. \end{cases} \quad (3)$$

- the effective radius $r_{\text{eff}} = 3 u_t / a_t$ $[\mu\text{m}]$ (4)

• the effective aspect ratio $a_{eff} = \frac{\int_{a_{min}}^{a_{max}} \int_{r_{min}}^{r_{max}} u(r, a) dr da}{u_t}$ (5)

194 • the aspect ratio width $a_{width} = \frac{\int_{a_{min}}^{a_{max}} (a - a_{eff})^2 \int_{r_{min}}^{r_{max}} u(r, a) dr da}{u_t}$ (6)

196 Note that r here plays the role of a radius of a fictitious spherical particle with equal volume to the actual spheroidal one.

198 The software package consists of three (main) graphical user interfaces (gui), serving different purposes:

- 200 • The SphInX Configurator, where all initial calculation parameters for the inversion are set, e.g. size distribution characteristics, lidar setup, mathematical parameter settings (methods, splines, interval partitions and simulation configurations). There is also the possibility of loading netcdf or ascii files with the optical parameters from measurement cases. This gui communicates all initializations to SphInX Main either directly or through user-stored configuration files.
- 202 • The SphInX Main, an independent gui where the inversion takes place. This gui is responsible for the resulting microphysical parameters, including visualizations (either real-time or on demand) of the shape-size distribution and the solution space. Owing to the structure of this gui with several mathematical parameters (e.g. regularization parameters), and illustrations of solution spaces, distributions and tabularized retrieval outcomes, here, 208 occur all preliminary tests which are vital for the main runs. This gui communicates all inversion products to SphInX MPP either directly or through user-stored configuration files.
- 210 • The SphInX MPP, an independent gui where all microphysical parameters are shown both 212 individually and briefly in tables with an error analysis, regarding accuracy (in case of simulations) and solution uncertainties. This gui focuses mainly on an a posteriori filtering and analysis of the inversion results.

214 SphInX operates with expendable pre-calculated discretization databases based on spline collocation and on look-up tables of scattering efficiencies using T-matrix theory (Rother and Kahnert, 2009). This is to avoid the computational cost which would otherwise limit the microphysical retrieval to an impractical point. When no information on the linear particle depolarization ratio (δ_{aer}) is given (usual setup “ $3\beta_{aer} + 2a_{aer}$ ”), the software runs using Mie theory. The inversion is done by regularization combined with a parameter choice rule. The following combinations are available:

- 224 (i) Truncated singular value decomposition (TSVD) with the discrepancy principle (DP),
- (ii) Tikhonov regularization with the L-curve method (LC),
- 226 (iii) Padé iteration with the discrepancy principle,
- (iv) Tikhonov regularization with the generalized cross validation method (GCV),
- 228 (v) Tikhonov regularization with the discrepancy principle, and
- (vi) Padé iteration with the L-curve

230 Details on the widely used methods TSVD and Tikhonov and the parameter choice rules DP, LC and GCV can be found in most books about regularization, for instance Hansen (2010). Padé iteration, in this context, is part of the so-called generalized Runge-Kutta regularization methods (see Böckmann and Kirsche, 2006).

234 The optical data profiles obtained from hourly averaged vertical profiles of the aerosol optical properties of Raman lidar observations were used as inputs for our inversions. This was done by specifying certain layers of interest and then averaging to produce the 6-point dataset of the so-called $3\beta_{aer} + 2a_{aer} + 1\delta_{aer}$ setup. These thin layers were selected in heights above the

238 atmospheric boundary layer, where the LR and AE values were varying slowly showing
240 homogeneity inside the plumes. The next step was to determine the initial parameters for the
retrieval using physical knowledge and/or inversion stability tests.

Such preliminary numerical tests revealed an overall superior behavior of the method Padé-DP as
242 compared to the other built-in methods. This motivated us to choose the Padé iterative
regularization method (Böckmann and Kirsche, 2006) for our measurement cases, in particular with
244 a fixed number of 30 iterations. Moreover, a strong tendency to shape-bimodality led us to use 6 -
8 spline points and the spline degrees 2 – 4 among the maximum available ranges of 3-20 and 2-6
246 respectively. The CRI is fed to the software separately for the real and imaginary parts which then
constitutes a grid combining the following default values: Real part (RRI)
248 [1.33, 1.4, 1.5, 1.6, 1.7, 1.8] and Imaginary part (IRI) [0, 0.001, 0.005, 0.01, 0.03, 0.05, 0.1].
Ideally, this grid can be further confined either when there is sufficient knowledge on aerosol
250 composition (or the exact CRI) and/or through numerical tests which indicate unstable or relatively
improbable solutions. For our study the CRI grid was narrowed down to (RRI [1.4, 1.5], IRI
252 [0, 0.001, 0.005, 0.01]). Extreme absorption (RRI=0.05 or 0.03) was ruled out mostly for the
following reasons. First, it is expected to manifest itself much less often for dust particles.
254 According to some reports on literature, such values can be found, for instance, directly on dust
site (see e.g. Wagner et al., 2012) or when the dust concentration is lower so that a soot-type
256 absorber prevails (see e.g. Schladitz et al., 2009). Therefore, while not improbable we consider
those cases much less encountered and not relevant to the presented cases. Second, preliminary
258 runs with higher IRI and/or lower RRI have shown that the resulted shape-size distributions are
less easily reconcilable physically, suggesting smoother representations and having undesired
260 systematic behavior. This is indeed an inherent issue of the inversion process since high IRI values
and/or low RRI values are known to smooth out the involved scattering cross sections, see e.g.
262 (Samaras, S., 2016; Rother and Kahnert, 2009) and lead to more severely ill-posed problems. Thus,
the risk to compromise further the retrieval combined with the relatively small likelihood of high
264 absorption outweighs the benefit here. Higher RRI values impose only a minute variation to the
results according to preliminary runs and thus excluded too.

266 The determination of the CRI grid is known to have a severe impact even for less complicated
schemes based on Mie theory and it is apparently applicable here since we add an additional
268 dimension (shape information) and simultaneously we restrict to coarser radius- and aspect ratio
ranges. However, massive simulations performed by Samaras (2016) for different atmospheric
270 scenarios showed that microphysical retrievals with an initially known CRI keep high accuracy and
small uncertainty levels. Furthermore, variations of the RRI have minor effects in the retrieved
272 parameters a_t , v_t , r_{eff} and variations of the IRI adds a relatively conservative percentage of 3-20%
to the uncertainties compared to the fixed-RI retrievals when the imposed measurement error is
274 reasonably contained. For the retrieval of the shape parameters, the situation is more complicated,
and simulations suggest that the quality of the results depend additionally on particle size. Detailed
276 implications of possible variations in shape (α), size (r), and composition (CRI) in the context of
simulations exceed the scope of this article and will be revisited exclusively in a future study as a
278 subject of great theoretical interest.

For the shape-size distribution we used a grid of 30×30 ($r \times a$) points with the radius $r \in$
280 $[0.01, 2.2]$ in μm and the aspect ratio $a \in [0.67, 1.5]$. While both ranges are the maximum available
in the software using the spheroid-particle approximation, there is no such (radius) restriction for
282 runs in “spherical” (Mie) mode in the software. Having specified the initial parameters, the
inversion is ready to take place and produce the volume shape-size distribution, the refractive index
284 and the parameters (1-6).

All methods in SphInX share a common algorithm primarily aiming to extract the unknown volume
286 shape-size distribution and calculate the rest of the parameters (except CRI) in a second step. First

288 the solution space has to be determined in terms of a specific spline point number and degree which
is normally a part of the aforementioned initial parameters. Instead, we only define loosely a range
290 for these parameters and run the inversion for every spline point number and degree within this
range and for every CRI. Then we make forward calculations for all solutions, and pick the one
CRI associated with the solution with the least residual error. We repeat the process for all spline
292 point numbers and degrees and order the solutions in decreasing quality order (residual-error-wise).
Finally, we calculate the mean solution (distribution and CRI) out of the first few least-residual
294 solutions and then the rest microphysical products using the equations (1-6). We will refer to the
selected solutions and the corresponding parameters as the “best”. This approach is based on hybrid
296 regularization methods described in detail in (Samaras et al. 2015; Samaras, 2016).

This algorithm allows for a straightforward uncertainty calculation. The Variability (Var %) of a
298 parameter here stands for the standard deviation of the selected best (least-residual) values, divided
by their mean value. If there are multiple datasets, then a mean variability is implied, i.e. Var is
300 found for each dataset and then their mean value is assigned to Var. Moreover, in the latter case,
the Uncertainty (*Unc %*) of a parameter is the ratio of the standard deviation of the mean values of
302 this parameter for each dataset over their mean. For simulations, the different datasets are usually
produced with random realizations of input error added to a synthetic dataset, and therefore *Unc* is
304 a measure of numerical stability. For measurement cases, these datasets could consist of optical
data values related to consecutive smaller “sub-layers” of a layer which is partitioned in order to
306 keep intensive parameters (e.g. AE, LR) relatively constant, and therefore *Unc* serves as an
additional measure of variability among the retrieved solutions.

308 3. Air mass analysis

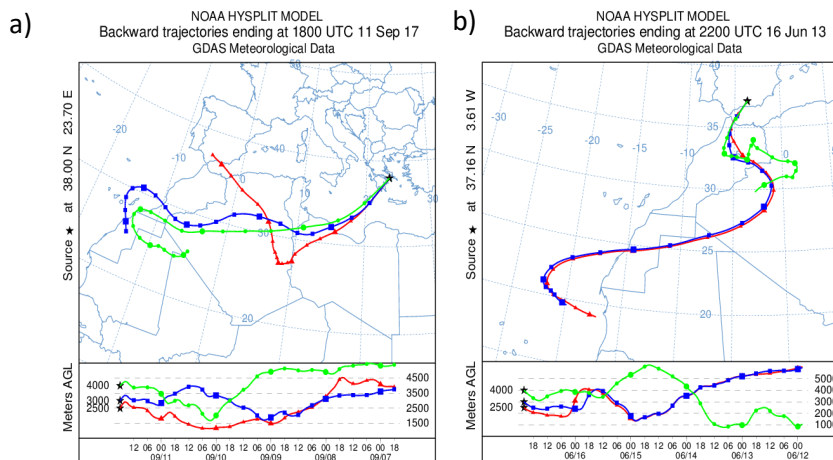
To verify that the source region of the air masses arriving over Athens and Granada, is originating
310 over the African continent, an analysis of backward trajectories was performed by means of the
HYSPLIT model (Hybrid Single-Particle Lagrangian Integrated Trajectory, Stein et al., 2015;
312 Rolph et al., 2017). All trajectories were calculated for a period of 120 hours backward in time and
were computed for arrival heights of approximately the bottom, center and top of the observed
314 layers. In this study, transport time refers to the time that the air masses travelled after leaving the
African continent and until they were detected over our stations. Based on this transport time, the
316 four selected dust cases reveal a pattern which allows us to separate them into two categories: (i)
transport time ≤ 1 day, which indicates quite pure or less mixed particles within the dust layer
318 (Figure 1), (ii) transport time > 1 day, which indicates a combination of mineral dust, polluted
mineral dust or even smoke arriving over the stations (Figure 2).

320 **i) Transport time (after African continent) ≤ 1 day:** The air mass backward trajectories arriving
over Athens on 11 September 2017 (case A), at 18:00 UTC, between 2-4 km (cf. Fig. 1 left), shows
322 that ~18 hours of the total of 120 hours of the residence time are spent over the Mediterranean Sea
and 60 (at 3000 m) to 100 hours (at 4000 m) over S. Morocco, Algeria and Libya, where Saharan
324 desert areas spread out. Similarly, for the air mass backward trajectories arriving over Granada on
16 June 2013 (case B), at 22:00 UTC, between 2.5-4 km, (cf. Fig. 1 right), ~24 hours are spent over
326 N. Morocco and Alboran Sea and 48 hours (at 2500 and 3000 m) over E. Morocco and Algeria,
areas that belong to the Saharan region. Consequently, the aforementioned air masses in both cases
328 are travelling quite fast (≤ 1 day), probably favoring the direct transport of mineral dust aerosols.

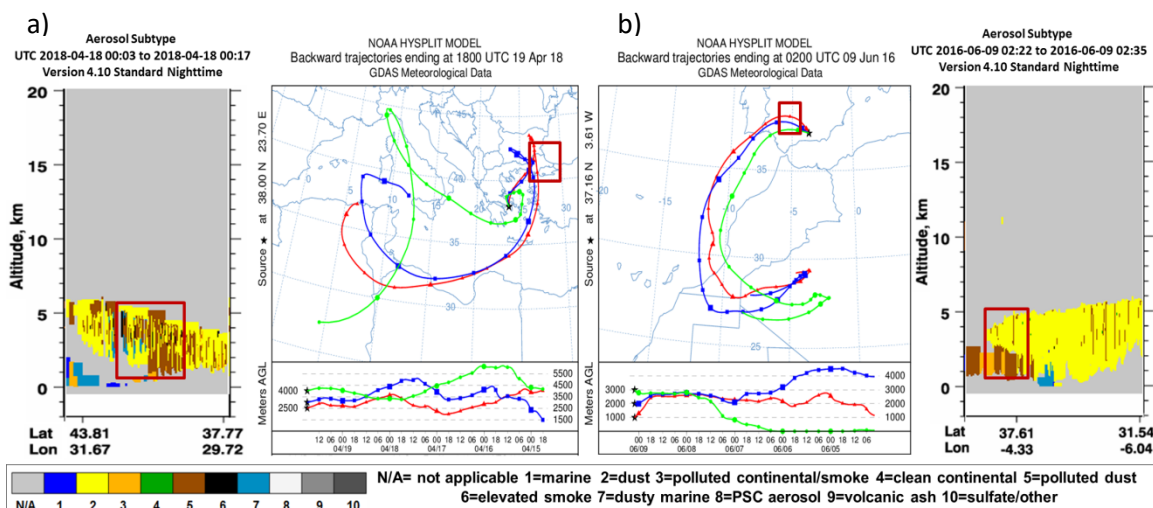
ii) Transport time (after African continent) > 1 day: For the case of 19 April 2018 detected over
330 Athens (case C), the air mass backward trajectories calculated at 18:00 UTC, show that less than
30 of the total 120 hours are spent over Libya and Tunisia while the rest 90 hours are spent
332 circulating over Mediterranean, Aegean Sea and Bulgaria (cf. Fig. 2 left). Analogously, for the case
of 9 June 2016 detected over Granada (case D), the calculated backward trajectories at 02:00 UTC,
334 show that ~48 of the total 120 hours are spent over the Atlantic Ocean and the Andalusian region

336 while the other 72 hours over S. Morocco and Algeria (cf. Fig. 2 right). It is evident that in both
338 those events, there is no direct air mass flow from the source region to the lidar stations, but an
alternative path above marine and urban areas. Therefore, the measured aerosol optical properties
for these cases can be attributed to a mixing state where industrial, marine or even biomass burning
aerosols were possibly mixed with the desert dust aerosols.

340 In order to investigate the possible mixing with other aerosol particle types during the air masses
transport, we used the observations of the spaceborne CALIOP (Cloud-Aerosol Lidar with
342 Orthogonal Polarization) to track the aerosol plumes for the cases of the second category. This lidar
system is onboard the CALIPSO (Cloud-Aerosol Lidar and Infrared Pathfinder Satellite
344 Observation) mission. In this work we used the aerosol typing product of (Kim et al., 2018). We
found CALIPSO overpasses that were intersecting the backward trajectories as presented in Figure
346 2 (red boxes). Using the aerosol typing mask, it was possible to determine the degree of mixing for
these two cases. It is easily observed that the air masses that eventually arrived over Athens at 19
348 April 2018 contained not only pure mineral dust, but also polluted dust and even some smoke
particles (yellow, brown and black colors respectively). Moreover, the case of 9 June 2016 shows
350 that mainly pure dust (above 3 km) and polluted dust (below 3 km) was transported over Granada.
Keeping this information in mind, we could expect different features in terms of optical and
352 microphysical properties for these two dust transport cases. It should be mentioned here that there
were no CALIPSO data available for case A and no overpass over Spain for case B, consequently
354 no such info is given for Figs. 1a and 1b.



356 Figure 1: 120-hour air mass backward trajectories arriving over a) Athens on 11/09/2017, (case A, 18:00 UTC), between
358 2-4 km height and b) Granada on 16/06/2013, (case B, 22:00 UTC), between 2.5-4 km height.



360 Figure 2: 120-hour backward trajectories over a) Athens on 19/04/2018, (case C, 18:00 UTC), between 2.5–4.5 km and
 362 b) Granada on 09/06/2016, (case D, 02:00 UTC), between 1–3 km height, along with position (altitude, latitude and
 364 longitude) and type of the aerosol layers detected by CALIOP during one overpass tracking the air masses contained
 within the red boxes (extreme left and right). Yellow and brown colors stand for pure and polluted dust respectively,
 while black indicates smoke.

4. Particle optical and microphysical characterization

366 In this section, the presented results pertain to i) columnar properties from AERONET retrievals,
 368 ii) vertical profiles of the aerosol optical properties from lidar data using Raman inversion
 algorithms and iii) microphysical properties from Raman lidar using the SphInX software. Since
 370 the AERONET derived aerosol size distributions refer to columnar values with aerosol radius
 ranging from 0.01 μm up to 15 μm and were performed earlier than the nighttime lidar
 372 measurements, no direct comparison with SphInX results is implemented. However, the coherence
 of results can be shown.

4.1. Column-integrated aerosol properties

374 The main direct AERONET products obtained for the relevant selected temporal windows are
 summarized in Table 1. The AOD at 500 nm was at least 0.27, with relatively low FMF values in
 376 all cases but C. In this case, the presence of polluted and smoke particles (see section 3) makes the
 fine and coarse mode (related to mineral dust) share similar proportions with a FMF of 55%. The
 378 spectral dependent AOD's and AE_{AOD} 's show values much lower than the usual for urban sites
 (e.g. Alados-Arboledas et al., 2003 and 2008; Lyamani et al., 2010; Gerasopoulos et al., 2011),
 380 again with the exception of case C, where AE value is close to 1, a representative value for mixed
 biomass burning with desert dust

382 aerosols (Giannakaki et al., 2016).

Table 1: Columnar properties retrieved from direct AERONET measurements.

Case	Time (UTC)	AOD (500 nm)	FMF (%)	AE_{AOD} (440/870 nm)
A) AT, 11/09/2017	15:36	0.34	22	0.22
B) GR, 16/06/2013	18:28	0.27	28	0.36
C) AT, 19/04/2018	15:20	0.27	55	0.94
D) GR, 09/06/2016	18:21	0.54	19	0.16

384

386 In order to characterize the aerosol particles in the atmospheric column in more detail, selected
 388 products provided by AERONET inversions (using AOD and sky radiance measurements) were
 analyzed. In Figure 3 (left), we can observe typical SSA values for dust particles increasing with
 390 wavelength, except case C, ranging from 0.85 to 0.98 as also observed by Dubovik et al. (2002),
 Valenzuela et al. (2012) and Benavent-Oltra et al. (2017). The IRI values (Figure 3 right), especially
 392 in case B, are a bit higher than the reported by Dubovik et al. (2002), but agree with those from
 Benavent-Oltra et al. (2017). The spectral behavior of these two variables (SSA, IRI) yields further
 394 interesting information. The cases with shorter transport time (case A and B) have similar positive
 slope for SSA and negative for IRI, as also reported in the literature (Toledano et al., 2011;
 Valenzuela et al., 2012; Lopatin et al., 2013; Schuster et al., 2016; Benavent-Oltra et al., 2017). For
 396 case C, where the dust was transported during longer time and there is a strong possibility of mixing
 with biomass burning particles, we can observe no dependence on wavelength (zero slope), a
 feature related to the presence of black carbon from combustion (Bergstrom et al., 2007). In case
 398 D, where again the transport process last longer, the spectral dependence is more pronounced in
 the shorter wavelengths showing similarities with cases A and B. These results suggest that the
 400 higher the element of dust and the contribution of larger particles in the mixing, the more
 pronounced spectral difference for smaller wavelengths. Moreover, absorption is lower and SSA is
 402 higher in general for the cases with more aged or mixed particles (cases C and D). It should be
 noted here that there have been numerous studies providing fundamental insights into the complex
 404 photochemistry of mineral dust aerosol in the atmosphere (Cwiertny et al., 2008). Liquid or
 adsorbed water and coatings can affect dust photochemistry as mineral dust particles are transported
 406 through the atmosphere, as well as the diurnal cycle can affect the mineral dust properties between
 daytime (AERONET) and nighttime (Raman-lidar) measurements.

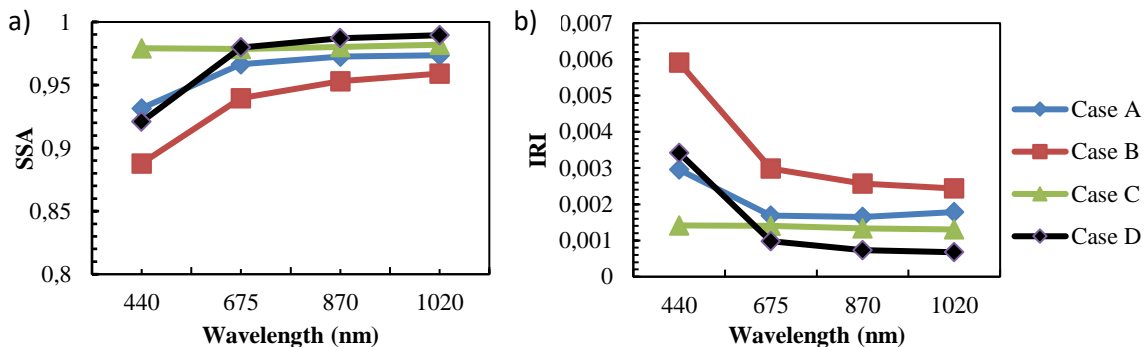
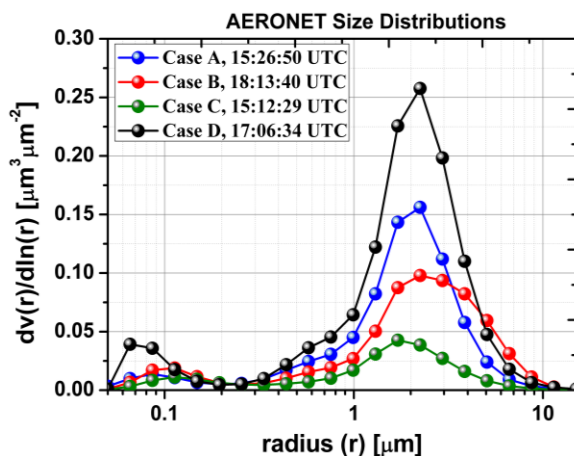


Figure 3: AERONET retrievals of a) SSA and b) IRI for cases A to D.

410 In all four studied cases, the size distributions retrieved by AERONET inversion code, showed
 again that the fine modes are not significant compared to the coarse modes that are dominant in the
 412 atmospheric column (Figure 4). This means a contribution of larger particles that corroborates the
 desert origin of the aerosols. The dominance of coarse mode particles is highlighted by the bimodal
 414 size distribution with separation radius ranging from 0.18 μm to 0.30 μm . For our first category
 (Cases A and B), the bi-modal volume size distributions have almost similar structure with low fine
 416 mode concentration ($< 0.02 \mu\text{m}^3/\mu\text{m}^2$). Specifically, for case B, the coarse mode is shifted to a bit
 larger radii while a small difference in maximum volume concentration equal to $0.06 \mu\text{m}^3/\mu\text{m}^2$
 418 indicates quite similar intensity of the events of cases A and B. For our second category (Cases C
 and D), a large difference in the size distributions between the two events is obvious. A high peak
 420 of coarse mode for case D in comparison to the lower concentration of case C represents a more
 intense dust episode. The highest intensity differences among the dust episodes are mostly reflected
 422 by the associated magnitudes of the volume concentration. For instance, the highest coarse-mode
 peak, corresponding to Case D, represents a relatively more intense dust episode as compared e.g.

424 to the lowest peak corresponding to case C. There are further differences to be observed regarding
 426 the shape of the coarse mode with the most evident one corresponding to the mode width, which is
 substantially greater for case D than for case C having ranges 0.33-8.65 μm and 0.44-6.64 μm
 respectively.



428

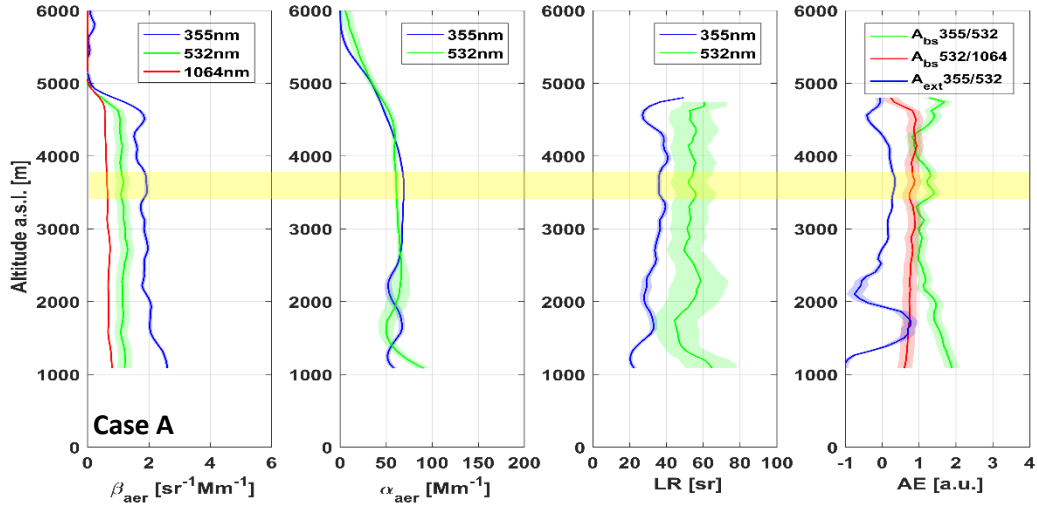
Figure 4: AERONET volume size distributions $dV(r)/d\ln(r)$ for cases A to D.

430 4.2. Vertically-resolved aerosol properties

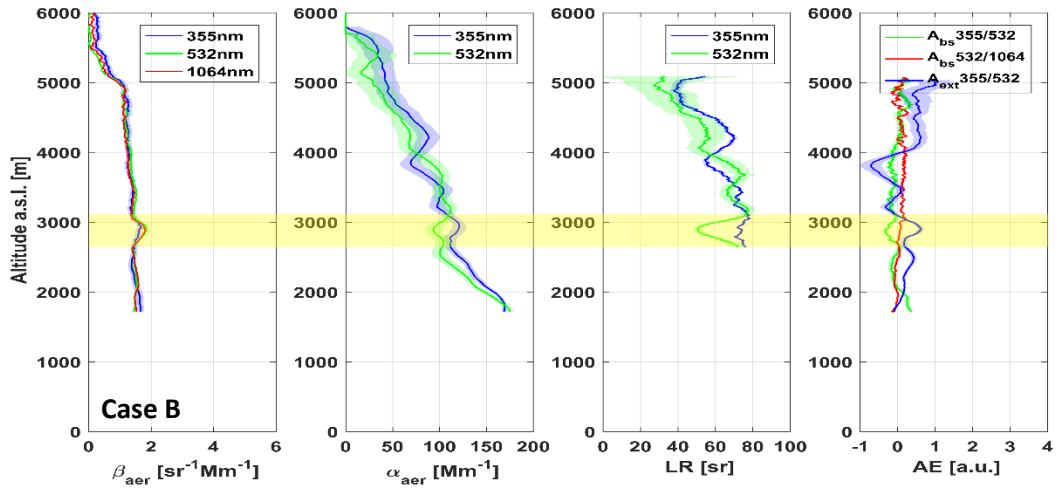
4.2.1. Optical properties

432 Figure 5 (a and b) depicts the vertical profiles of the dust aerosol optical properties of the two
 independent mineral dust cases A and B. On 11 September 2017 (Fig. 5a) a thick, intense and
 434 almost uniform dust layer from around ground level up to 4.5 km height (a.s.l.) was detected by
 EOLE [17:00-18:30 UTC] over Athens. On 16 June 2013 (Fig. 5b) there is an almost uniform layer
 436 in the atmospheric column above Granada, which, similarly to case A is reaching 4.7 km above
 ground level [22:00-22:30 UTC]. For the aforementioned cases we selected the thin layers 3.5-3.8
 438 and 2.65-3.1 km a.s.l. respectively. The selection of these thin layers inside the dust plumes was
 based not only on the homogeneity of the optical properties, but also on the backward trajectories
 440 in which, at roughly these altitudes, the source region is the same (W. Algeria) as shown in Fig. 1.
 The vertical profiles of the other two cases representing events of more aged and mixed dust layers
 442 are also presented in Fig. 5 (c and d). At least two decoupled aerosol layers of different intensities
 are detected over Athens on 19 April 2018 (Fig. 5c) between 1.5 and 4.5 km a.s.l. [17:30-18:50
 444 UTC]. The vertical profiles on 9 June 2016 in Granada (Fig. 5d) confirm the decoupled thick
 mineral dust layer of different intensities, between 2.5 and 5 km a.s.l. Here, we selected the thin
 446 layers 2.6-2.8 [17:30-18:50 UTC] and 2.55-2.75 km a.s.l. [01:00-02:00 UTC] respectively in which
 there was indication of mixed layers; polluted dust or even smoke particles for case C, polluted
 448 dust for case D (see also Fig. 2).

a)

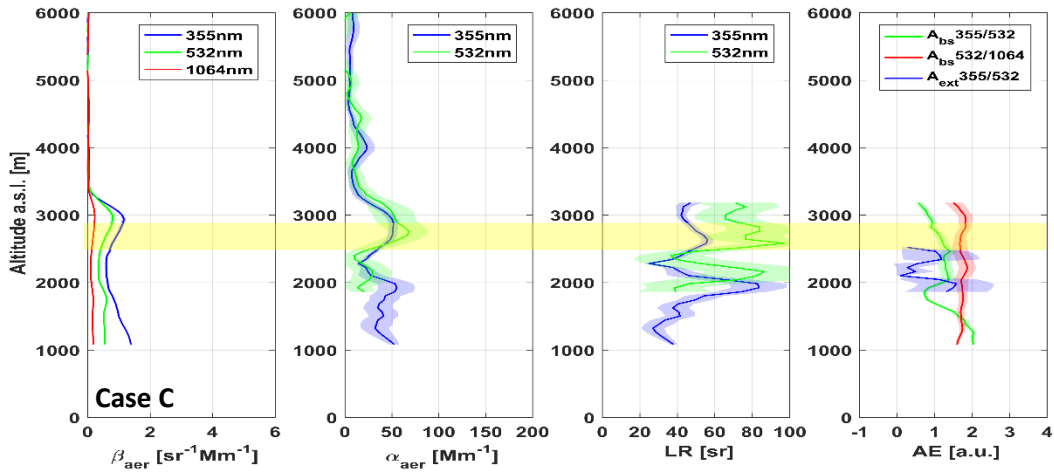


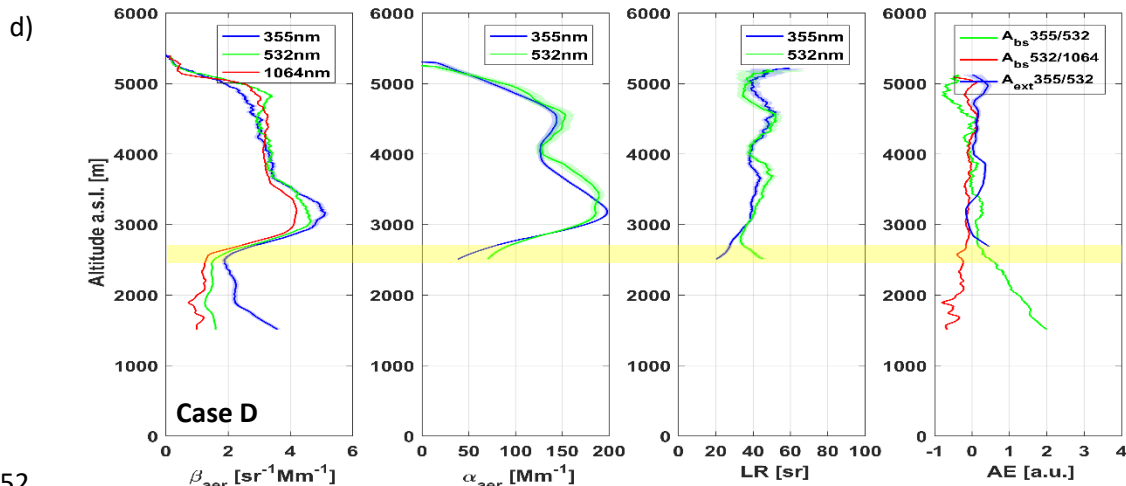
b)



450

c)





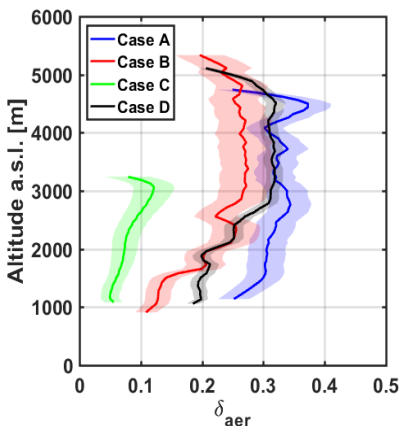
452

454 Figure 5: Vertical profiles of the aerosol optical properties (β_{aer} , α_{aer} , LR, AE) obtained over a) Athens on 11 September
 455 2017, 17:00-18:30 UTC (Case A), b) Granada on 16 June 2013, 22:00-22:30 UTC (Case B), c) Athens on 19 April 2018,
 456 17:30-18:50 UTC (case C), between and d) Granada on 9 June 2016, 01:00-02:00 UTC (case D) along with their error
 estimations (horizontal bounds). Yellow layers indicate the regions selected for microphysical analysis.

458 Within all four selected aerosol layers of our independent cases studied here, the mean values of the optical properties obtained from the lidar measurements and used for the inversions are shown in Table 2, along with their standard deviation. Their intensive parameters are also presented. For the first two cases (A and B) with transport time less than one day these values represent the typical optical properties of short range transported dust plumes. More specifically, typical LR values were found (54 \pm 1 and 64 \pm 6 sr at 532 nm respectively) falling within the ranges for Saharan-dust particles found in literature (Müller et al., 2009; Groß et al., 2011). The backscatter related AE (AE_{b532/1064}) values of 0.83 \pm 0.04 and 0.03 \pm 0.02 respectively correspond to quite large particles in accordance with previous findings (Mamouri and Ansmann, 2014; Veselovskii et al., 2016). The small standard deviation values underline that aerosol particles were well mixed in the altitude range of the uniform dust layers. Concerning the remaining two cases (C and D) we found larger deviations among their intensive optical properties. Quite high mean LR value of 79 \pm 5 sr (at 532 nm) for case C corroborate the strong indication that dust particles were mixed with particles of other origins such as smoke while travelling. Lower LR values of 39 \pm 2 sr (at 532 nm) for case D. Contrary to the category with transport time up to one day, here, the decoupled plumes were probably relatively inhomogeneously distributed along the vertical direction and mixed with aerosols from different origins (possible biomass burning mixtures for case C and polluted mixtures for case D) or even different regions in Sahara desert (differences in chemical composition of the mineral dust).

476 Figure 6 presents the vertical profiles of δ_{aer} of the four case studies (at 355 nm for Athens and at
 478 532 nm for Granada system). Typical values of desert dust δ_{aer} (Freudenthaler et al., 2009, Groß et
 al., 2015), were calculated for the cases of the first category, verifying again the dominance of the
 480 mineral particles. More specifically, mean δ_{aer} values equal to 0.34 \pm 0.02 for case A (17:30-18:30
 UTC, 3.5-3.8 km) and 0.26 \pm 0.04 for case B (22:00-22:30 UTC, 2.65-3.10 km)) provide a clear
 482 indication of the non-sphericity of the pure dust particles. For these cases, the particles of mineral
 dust sources seem to be rather unaffected by anthropogenic or other polluted aerosols. For the cases
 484 of the second category, the mean δ_{aer} calculated inside the plumes show marginal standard
 deviation. The value of δ_{aer} was found equal to 0.11 \pm 0.01 for case C (17:30-18:30 UTC, 2.6-2.8
 km) and 0.28 \pm 0.01 for case D (01:00-02:00 UTC, 2.55-2.75 km). The fact that in case D the
 486 value of δ_{aer} increases above 2.5 km a.s.l. ($\delta_{\text{aer}} = 0.32 \pm 0.01$, 3-4.5 km) confirms the separation
 between polluted and pure dust layers observed by CALIPSO (see Fig. 2b). Moreover, the

488 aforementioned influence of mixtures (dust and smoke) can explain the lower δ_{aer} values of around
 490 10% calculated for case C, which are in accordance with previous studies (Ansmann et al., 2011;
 Groß et al., 2011; Tesche et al., 2011; Wandinger et al., 2016; Giannakaki et al., 2016).



492 Figure 6: Vertical profiles of the δ_{aer} for cases A to D along with their error estimations (horizontal bounds). For Athens
 and Granada stations depolarization measurements are available at 355 nm and at 532 nm respectively.

494 4.2.2. Microphysical properties

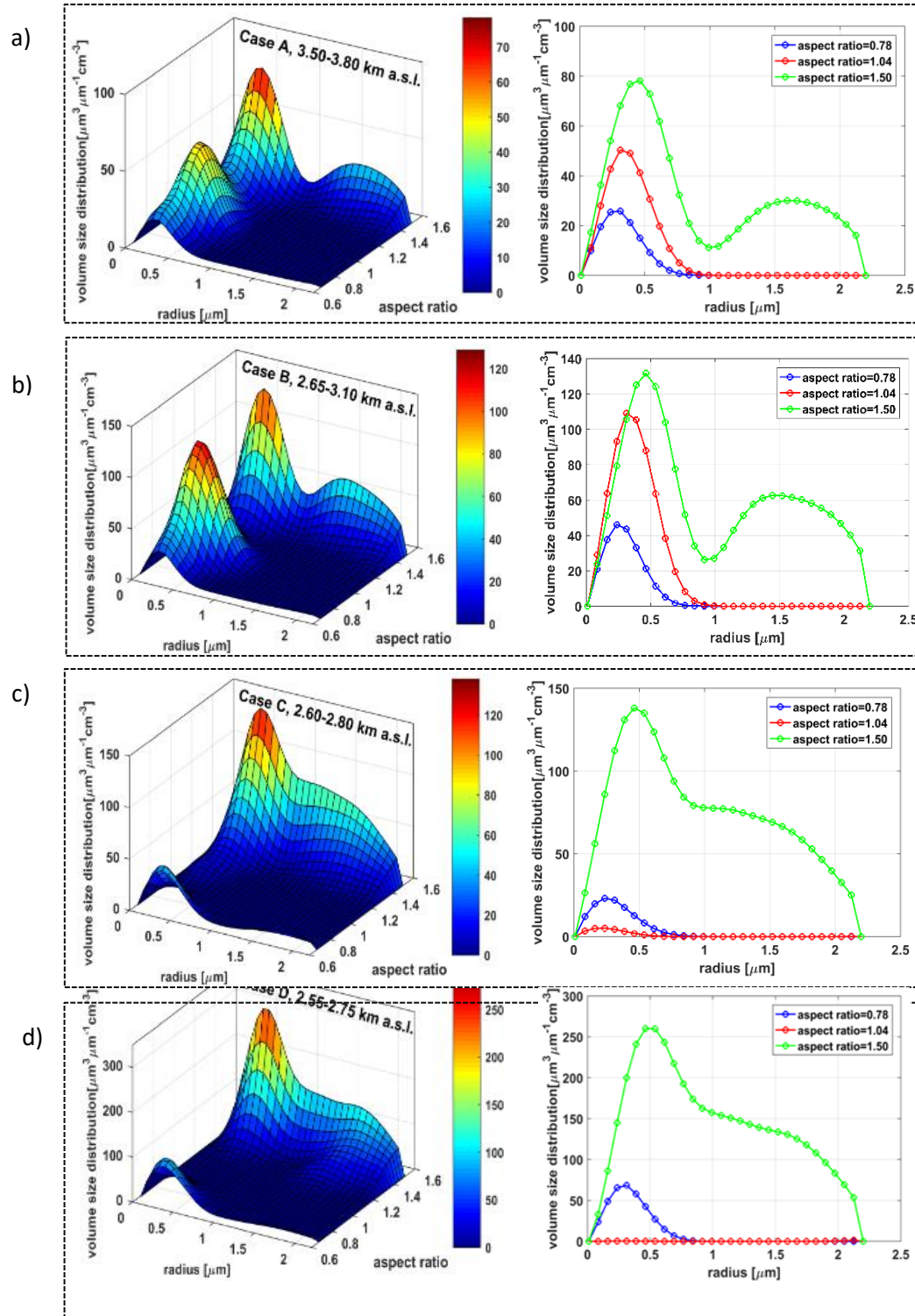
For each selected dust layer, the SphInX inversion algorithm was applied using the mean values of
 496 our optical datasets analyzed in Table 2 as inputs. Table 3 shows the average values of a_r , u_t , r_{eff} ,
 a_{eff} and α_{width} , RRI, IRI and SSA, along with their Var (%) derived by using the 5 best solutions
 498 picked by the software according to the algorithm described previously.

The RI for the mineral dust cases of the first category is found equal to $1.4 + 0.004i$ inside both
 500 selected layers and SSA (532 nm) equal to 0.97 for case A and 0.98 for case B, which points to
 weakly absorbing particles. On the other hand, different values of the CRIs were found for the cases
 502 of the second category. More specifically, for case C the CRI was found equal to $1.5 + 0.002i$ while
 for case D it was found equal to $1.5 + 0.005i$.

504 For the less mixed dust episodes the retrieved 2D shape-size distributions reveal the same three-
 mode pattern (Figs. 7 a and b). Two of the three modes correspond to prolate particles ($a \approx 1.5$),
 506 confirming the non-spherical nature of the dust particles. The prolate particle modes can be
 subdivided into a coarse mode with radii $r \approx 1.7 \mu\text{m}$ and a fine mode around $0.5 \mu\text{m}$. A third
 508 mode centered in $a \approx 1$ and $r \approx 0.3 \mu\text{m}$ represents an additional contribution of spherical
 particles. The effective radius for the more intense episode of case A is found shifted to larger
 510 values ($0.57 \pm 0.05 \mu\text{m}$) as compared to the corresponding case B ($0.33 \pm 0.02 \mu\text{m}$).

In Fig. 7c, the dominant mode of the shape-size distribution corresponds to prolate fine particles
 512 (up to $a \approx 1.5$, $r \approx 0.5 \mu\text{m}$) and is extended up to $2.2 \mu\text{m}$. There is a less prominent but
 substantially wider mode pertaining to prolate coarse particles (up to $a \approx 1.5$, $r \approx 1.4 \mu\text{m}$) with
 514 a less obvious separation point. Furthermore, the smaller peak indicates a contribution of oblate
 fine particles ($a \approx 0.7$, $r \approx 0.3 \mu\text{m}$). However, due to the relatively low magnitude of this peak
 516 and the possibility of oversmoothing of the prolate coarse mode, the case that this peak might be
 either a suppressed larger peak or an artifact, should be considered as well. In Fig. 7d, the dominant
 518 mode of the shape-size distribution has similar behavior with the one of case C concerning the
 prolate fine mode (up to $a \approx 1.5$, $r \approx 0.5 \mu\text{m}$, extended up to $2.2 \mu\text{m}$). However, the less
 520 prominent mode pertaining again to prolate coarse particles seems to be extended to smaller α
 values ($a \approx 1.3$, $r \approx 1.5 \mu\text{m}$). Here, there is a more significant coarse mode contribution in
 522 accordance with the higher δ_{aer} value compared to case C. For these four cases the dust particles

524 behave effectively as prolate spheroids as it is further indicated by the values of α_{eff} ranging between
 526 1.19 – 1.32 (see Table 3). The value of a_{width} was calculated equal to 0.06 ± 0.01 for all cases.
 528 The differences in the shape size distributions for the cases presented in Fig. 7 provide an additional
 indication for differences in aerosol composition occurring due to the different travelled path bound
 to each case. Since case D owns the most intensive event (see Figure 5) it takes the greatest u_t value
 equal to $37 \mu\text{m}^3\text{cm}^{-3}$, while for the rest cases A, B and C we have 16, 29, and $20 \mu\text{m}^3\text{cm}^{-3}$
 respectively (see Table 3).



530 Figure 7: The shape-size distribution shown in 3D (left) for the hole aspect ratio range and in 2D (right) for 3selected
 532 aspect ratio values (0.78-oblate, 1.04-spherical, 1.50-prolate particles) for a) case A at 3.5-3.8 km a.s.l., b) case B at
 2.65-3.10 km a.s.l., c) case C at 2.6-2.8 km a.s.l. and d) case D at 2.55-2.75 km a.s.l. as retrieved by SphInX software
 tool.

534 Table 2: Average particle optical properties for the selected thin layers within the dust zone along with their standard
 deviation.

Case		A	B	C	D
Layer height a.s.l. [km]		3.50-3.80	2.65-3.10	2.60-2.80	2.55-2.75
Optical properties	α_{355} [Mm^{-1}]	68.62±0.89	115.60 ±6.94	49.11±3.13	62.27 ±1.62
	β_{355} [$\text{Mm}^{-1} \text{sr}^{-1}$]	1.89±0.06	1.55±0.11	0.94±0.11	2.39 ±0.43
	α_{532} [Mm^{-1}]	60.69±0.52	100.88±8.35	52.54±9.00	82.67 ±10.06
	β_{532} [$\text{Mm}^{-1} \text{sr}^{-1}$]	1.13±0.03	1.67±0.06	0.61±0.10	2.15 ±0.05
	β_{1064} [$\text{Mm}^{-1} \text{sr}^{-1}$]	0.63±0.01	1.621±0.001	0.18±0.02	1.83±0.05
	$\delta_{\text{aer } 355, 532}$	0.34±0.02	0.26±0.04	0.11±0.01	0.28±0.01
Intensive properties	LR355 [sr]	36±1	76±7	51±4	28±4
	LR532 [sr]	54±1	64±6	79±5	39±2
	$A_{\text{ep } 532/1064}$	0.83±0.04	0.03±0.02	1.70±0.20	0.25±0.10

536

538 Table 3: Average particle microphysical properties for the selected thin layers along with their Var (%) (see Section 2),
 based on the 5 best solutions picked by the software.

Case		A	B	C	D
Layer height a.s.l. [km]		3.50-3.80	2.65-3.10	2.60-2.80	2.55-2.75
Lidar-based inversions	a_t [$\mu\text{m}^2\text{cm}^{-3}$]	152.20±8%	268.30±10%	140.99±3%	228.73±5%
	u_t [$\mu\text{m}^3\text{cm}^{-3}$]	16.13±10%	29.42±13%	19.92±8%	36.64±6%
	r_{eff} [μm]	0.32±4%	0.33±3%	0.42±8%	0.48±8%
	α_{eff}	1.18±5%	1.14±5%	1.32±1%	1.32±1%
	α_{width}	0.06±24%	0.06±25%	0.06±15%	0.06±25%
	Distribution uncertainty [%]	48.19	46.31	26.86	23.85
Microphysical properties	RRI	1.4±0%	1.4±0%	1.5±0%	1.5±0%
	IRI	0.004±43%	0.004±57%	0.002±50%	0.005±42%
	SSA [532 nm]	0.97±1%	0.98±2%	0.98±2%	0.96±2%

540 Restricting to a one-dimensional size distribution would offer a short-sighted view. If we picture,
 542 for instance, all aspect ratio contributions summed for the distributions in Fig. 7 (a,b,c,d) so that
 there is only radius dependence left, then the figures would appear relatively similar in trend
 544 qualitatively. Obviously, even the spheroidal consideration of dust particles does not capture the
 particle form physically (it is mainly a better fit for the observed optical properties), but with the
 546 described approach our analysis can be refined to include possible diversity among cases of interest
 which is otherwise invisible.

548 Although these 2D particle distributions provide more information than a usual size distribution
 there are also limitations to this approach which might affect the inversion outcome. Since there
 are several assumptions pertaining to the whole inversion chain (discretization, regularization, T-
 550 matrix theory etc.), a full discussion exceeds the scope of this article and will limit itself to some
 evident remarks. The less pronounced separation between fine and coarse modes especially for the
 552 prolate part in Fig. 7 might indicate higher measurement errors which were misidentified by

554 regularization; this is a common encounter also for the usual one-dimensional (size) distributions,
(see Samaras et al, 2015). The higher aspect ratio end (1.5) might not be sufficient in order to reveal
556 the full extent of the shape size distribution further along the aspect ratio axis. The same is true for
the radius boundary on the right end even though in our cases the distributions are only mildly
558 abrupt in this respect. Finally, the presence of potential small artifacts in the distribution, like for
instance in Fig. 7 (c and d) has only small contribution to the derived microphysical parameters
since the double integration suppresses further small oscillations in the solution.

560 The results obtained in this study (Tables 2, 3) can be compared with other values found in the
literature about transported Saharan dust events detected over Europe, Morocco and Cape Verde as
562 summarized in Table 4.

Table 4: Optical and microphysical properties found in the literature about transported Saharan dust events detected in Europe, Morocco and Cape Verde used to compare with the obtained values in Tables 2 and 3.

Reference	Region	Technique	Type	LR (λ)	β -AE (λ)	α -AE (λ)	δp (λ)	RRI (λ)	IRI (λ)	SSA (λ)	r_{eff}
(Mattis et al., 2002b)	Leipzig (51.3° N, 12.4° E)	Lidar	Dust	60 – 100 sr (355 nm) 50 – 80 sr (532 nm)			0.15 – 0.25 (532 nm)				
(Papayannis et al., 2005)	Athens (37.9° N, 23.8° E)	Lidar	Dust	53±1 sr (355nm)							
(Guerrero-Rascado et al., 2008)	Granada (37.16° N, 3.61° W)	Lidar	Dust	41 – 45 sr (532 nm)			0.15 – 0.25 (532 nm)				
(Guerrero-Rascado et al., 2009a)	Granada (37.16° N, 3.61° W)	Lidar	Dust	50 – 65 sr (532 nm)	-0.4 -0.5 (355/532 nm)						
(Freudenthaler et al., 2009b)	Quarzazate, Morocco (30.94° N, 6.91° W)	Lidar	Pure dust				0.26±0.06 (355 nm) 0.30±0.00 (532 nm) 0.28±0.05 (710 nm) 0.27±0.04 (1064 nm)				
(Petzold et al., 2009)	S Morocco (30.93° N, 6.91° W)	In Situ	Dust					1.550 – 1.565 (450 nm) 1.549 – 1.561 (550 nm) 1.546 -1.555 (700 nm)	0.0031 – 0.0052 (450 nm) 0.0016 – 0.0042 (550 nm) 0.0003 – 0.0025 (700 nm)		
(Córdoba-Jabonero et al., 2011)	Santa Cruz de Tenerife (28.5° N, 16.2° W); El Arenosillo (37.1°N, 6.7° W); Granada (37.16° N, 3.61° W)	Lidar and In situ	Pure dust	45 -70 sr (532 nm)							0.10 -0.15 μ m (fine) 1.06 – 1.72 μ m (coarse)
(Bauer et al., 2011)	Praia, Cape Verde (14.95° N, 23.49° W)	In Situ	Pure dust							0.92±0.07 (532 nm)	
(Groß et al., 2011b)	Praia, Cape Verde (14.95° N, 23.49° E)	Lidar	Dust	58±7 sr (355 nm) 62±5 sr (532 nm)			0.25±0.03 (355 nm) 0.30±0.01 (532 nm)				

(Tesche et al., 2011)	Praia, Cape Verde (14.95° N, 23.49° E)	Lidar	Dust	53±10 sr (355, 532 nm)	0.2±0.3 (355/532 nm) 0.45±0.16 (532/1064 nm)	0.2±0.3 (355/532 nm)	0.31 – 0.10 (532 nm) 0.37±0.07 (710 nm)				
(Tesche et al., 2011)	Praia, Cape Verde (14.95° N, 23.49° E)	Lidar	Dust/smoke	67±14 sr (355, 532 nm)	0.7±0.3 (355/532 nm, 532/1064 nm)	0.7±0.4 (355/532 nm)	0.15 – 0.05 (532 nm) 0.2±0.1 (710 nm)				
(Weinzierl et al., 2011)	Praia, Cape Verde (14.95° N, 23.49° E)	In situ	Dust					1.550±0.002 (467 nm) 1.550±0.002 (530 nm) 1.546±0.002 (660 nm)	0.004±0.002 (467 nm) 0.003±0.002 (530 nm) 0.001 ± 0.001 (660 nm)		1.21±0.32 μm
(Weinzierl et al., 2011)	Praia, Cape Verde (14.95° N, 23.49° E)	Lidar	Dust	42±5 sr (532 nm)			0.22±0.04				
(Toledano et al., 2011)	Praia, Cape Verde (14.95° N, 23.49° E)	Photometry								0.93±0.01 (440 nm) 0.98 – 0.99 (670, 1020 nm)	
(Preißler et al., 2011)	Évora (38.57° N, 7.91° W)	Lidar	Dust	45±11 sr (355 nm) 53±7 (532 nm)	0.4±0.6 (355/532 nm) 0.4±0.2 (532/1064 nm)	0.0±0.2 (355/532 nm)	0.28±0.04 (532 nm)				
(Valenzuela et al., 2014)	Alborán Island (35.95° N, 3.03° W)	Photometry								0.88±0.03 (440 nm) 0.91±0.03 (1020 nm)	
(Bravo-Aranda et al., 2015)	Granada (37.16° N, 3.61° W)	Lidar	Dust		0.8±0.1 (355/532 nm)		0.19±0.03 (532 nm)				
(Denjean et al., 2016)	Western Mediterranean Basin	Airborne In situ	Dust					1.50 – 1.55 (530 nm)	0.000 – 0.005 (530 nm)	0.90 – 1.00 (530 nm)	
(Benavent-Oltra et al., 2017b)	Granada (37.16° N, 3.61° W)	Lidar and Photometry	Dust		0.5±0.2 (532/1064 nm)			1.52 – 1.55 [355, 1064 nm]	0.001 – 0.013 (355 nm) 0.002 – 0.004 (640 nm) 0.001 – 0.003 (1064 nm)	0.86 – 0.95 (355 nm) 0.90 – 0.96 (640 nm) 0.96 – 0.99 (1064 nm)	0.10 -0.13 μm (fine) 2.2 – 2.4 μm (coarse)

566 5. Summary

568 During strong Saharan dust events that occurred over Athens and Granada, selected lidar
570 measurements were performed to retrieve the optical properties of dust particles in the lower free
572 troposphere. The cases were separated into two categories based on their transport duration time
574 focusing on short range (pure) to long range (mixture) dust processes. This categorization was
576 based mainly on the air mass back-trajectories from HYSPLIT model that were pointing to the
Saharan desert. CALIPSO data provided further information about the aerosol typing. The SphInX
software tool was used to derive the mean microphysical properties of dust particles for the four
independent dust events selected here running with $3\beta_{aer} + 2a_{aer} + 1\delta_{aer}$ input datasets. Padé
method with fixed iteration equal to 30 was chosen for the inversion among the other available
methods in SphInX on the basis of preliminary runs which favored its suitability.

Similarities were found between the cases A and B of the first category (transport time ≤ 1 day
with origin W. Algeria) concerning the optical properties (LR 54 ± 1 sr and 64 ± 6 sr at 532 nm
respectively), the shape size distribution, the RI values ($1.4 + 0.004i$ in both dust cases) and the
aspect ratio ($a_{eff} = 1.19$ and $a_{width} = 0.06$). On the contrary, there are differences in the
aforementioned parameters among the two categories. The LR values are higher for the more mixed
case C and lower for the long range transported case D (79 ± 5 sr and 39 ± 2 sr, at 532 nm
respectively). The mean $AE_{b532/1064}$ ranges within 0.03-0.83 for the less mixed cases indicating quite
large particles, while it is equal to 1.7 for polluted dust mixed with smoke. Moreover, the mean δ_{aer}
ranges from 11 to 34%, for the cases A, B and C, D depending on the aerosol composition. This
variability is expected not only because of the different Saharan region but also because of the
different path travelled (Balkans for case C and over Atlantic for case D) which further translates
to different aging and mixing processes. The retrieved RI values were found equal to $1.5 + 0.002i$
for case C and $1.5 + 0.005i$ for case D, while a_{eff} values around 1.32 for both cases pertaining
to volume size distributions mainly with prolate particles.

Selected column-integrated aerosol properties were also presented for a comprehensive analysis.
High AOD values (at 500 nm) were shown ranging from 0.27 to 0.54, depending on the intensity
of each event, while the calculated FMF (19-55%) and the spectral dependence of SSA and IRI
revealed the impact of the different aerosol types in terms of mixing.

In spite of the apparent limitations (restricted aspect ratio/radius domain) of this approach it was
demonstrated that the microphysical problem for non-spherical particles can be successfully
addressed. Moreover, the 2D volume distributions offer a new and more informative take on the
characterization of aerosols with respect to size and shape which further provides insight for the
particle mixing in this respect. Additional studies based on multi-wavelength lidar data using
SphInX software tool are suggested to be performed so as to improve our knowledge on the aging
and mixing aerosol processes and to enrich the aerosol microphysical properties database over
Southern Europe.

Acknowledgments

O. S.'s research project has been financed through a scholarship from the General Secretariat for
Research and Technology (GSRT) and the Hellenic Foundation for Research and Innovation
(HFRI). The co-authors from the University of Granada were mainly supported by the Spanish
Ministry of Sciences, Innovation and Universities through project CGL2016-81092, by the Spanish
Ministry of Education, Culture and Sports through grant FPU14/03684 and by the University of
Granada through the contract "Plan Propio. Programa 9. Convocatoria 2013". The financial support
for EARLINET in the ACTRIS Research Infrastructure Project by the European Union's Horizon
2020 research and innovation program under grant agreement no. 654169 is gratefully
acknowledged. O.S. and P. O-A. were further supported by the Erasmus+ programme of the

614 European Union. The authors thankfully acknowledge the FEDER program for the instrumentation
used in this work.

616 **References**

- 618 Alados-Arboledas, L., Alcántara, A., Olmo, F.J., Martínez-Lozano, J.A., Estellés, V., Cachorro,
V., Silva, A.M., Horvath, H., Gangl, M., Díaz, A., Pujadas, M., Lorente, J., Labajo, A.,
620 Sorribas, M., Pavese, G., 2008. Aerosol columnar properties retrieved from CIMEL
radiometers during VELETA 2002. *Atmos. Environ.* 42, 2654–2667.
<https://doi.org/10.1016/j.atmosenv.2007.10.006>
- 622 Alados-Arboledas, L., Lyamani, H., Olmo, F.J., 2003. Aerosol size properties at Armilla,
Granada (Spain). *Q. J. R. Meteorol. Soc.* 129, 1395–1413. <https://doi.org/10.1256/qj.01.207>
- 624 Amiridis, V., Balis, D.S., Kazadzis, S., Bais, A., Giannakaki, E., Papayannis, A., Zerefos, C.,
2005. Four year aerosol observations with a Raman lidar at Thessaloniki, Greece, in the
626 framework of European Aerosol Research Lidar Network (EARLINET). *J. Geophys. Res.*
Atmos. 110. <https://doi.org/10.1029/2005JD006190>
- 628 Ansmann, A., Petzold, A., Kandler, K., Tegen, I., Wendisch, M., Müller, D., Weinzierl, B.,
Müller, T., Heintzenberg, J., 2011. Saharan Mineral Dust Experiments SAMUM-1 and
630 SAMUM-2: What have we learned? *Tellus, Ser. B Chem. Phys. Meteorol.* 63, 403–429.
<https://doi.org/10.1111/j.1600-0889.2011.00555.x>
- 632 Ansmann, A., Riebesell, M., Wandinger, U., Weitkamp, C., Voss, E., Lahmann, W., Michaelis,
W., 1992. Combined Raman Elastic-Backscatter LIDAR for Vertical Profiling of Moisture,
634 Aerosol Extinction, Backscatter, and LIDAR Ratio. *Appl. Phys. B* 55, 18–28.
- Atkinson, James D; Murray, Benjamin J; Woodhouse, Matthew T; Whale, Thomas F; Baustian,
636 K.J. et al., 2013. The importance of feldspar for ice nucleation by mineral dust in mixed-
phase clouds - ProQuest. *Nature* 498.
- 638 Balis, D., Amiridis, V., Kazadzis, S., Papayannis, A., Tsaknakis, G., Tzortzakis, S., Kalivitis, N.,
Vrekoussis, M., Kanakidou, M., Mihalopoulos, N., Chourdakis, G., Nickovic, S., Perez, C.,
640 Baldasano, J., Drakakis, M., 2006. Optical characteristics of desert dust over the East
Mediterranean during summer. *Ann. Geophys.* 24.
- 642 Balis, D.S., Amiridis, V., Nickovic, S., Papayannis, A., Zerefos, C., 2004. Optical properties of
Saharan dust layers as detected by a Raman lidar at Thessaloniki, Greece. *Geophys. Res.*
644 *Lett.* 31, 10–13. <https://doi.org/10.1029/2004GL019881>
- Bauer, S., Bierwirth, E., Esselborn, M., Petzold, A., Macke, A., Trautmann, T., Wendisch, M.,
646 2011. Airborne spectral radiation measurements to derive solar radiative forcing of Saharan
dust mixed with biomass burning smoke particles. *Tellus, Ser. B Chem. Phys. Meteorol.* 63,
648 742–750. <https://doi.org/10.1111/j.1600-0889.2011.00567.x>
- Benavent-Oltra, J.A., Román, R., Granados-Munõz, M.J., Pérez-Ramírez, D., Ortiz-Amezcuca, P.,
650 Denjean, C., Lopatin, A., Lyamani, H., Torres, B., Guerrero-Rascado, J.L., Fuertes, D.,
Dubovik, O., Chaikovsky, A., Olmo, F.J., Mallet, M., Alados-Arboledas, L., 2017a.
652 Comparative assessment of GRASP algorithm for a dust event over Granada (Spain) during
ChArMEX-ADRIMED 2013 campaign. *Atmos. Meas. Tech.* 10, 4439–4457.
654 <https://doi.org/10.5194/amt-10-4439-2017>
- Dubovik, O., Chaikovsky, A., Olmo, F.J., Mallet, M., Alados-Arboledas, L., 2017b. Comparative
656 assessment of GRASP algorithm for a dust event over Granada (Spain) during ChArMEX-

- ADRIDMED 2013 campaign. *Atmos. Meas. Tech.* <https://doi.org/10.5194/amt-10-4439-2017>
- 658 Bergstrom, R.W., Pilewskie, P., Russell, P.B., Redemann, J., Bond, T.C., Quinn, P.K., Sierau, B.,
2007. Spectral absorption properties of atmospheric aerosols. *Atmos. Chem. Phys.* 7, 5937–
660 5943. <https://doi.org/10.5194/acp-7-5937-2007>
- Böckmann, C., Kirsche, A., 2006. Iterative regularization method for lidar remote sensing.
662 *Comput. Phys. Commun.* 174, 607–615. <https://doi.org/10.1016/j.cpc.2005.12.019>
- Böckmann, C., Mironova, I., Müller, D., Schneidenbach, L., Nessler, R., 2005. Microphysical
664 aerosol parameters from multiwavelength lidar. *J. Opt. Soc. Am. A* 22, 518.
<https://doi.org/10.1364/JOSAA.22.000518>
- 666 Böckmann, C., Osterloh, L., 2014. Runge-Kutta type regularization method for inversion of
spheroidal particle distribution from limited optical data. *Inverse Probl. Sci. Eng.* 22, 150–
668 165. <https://doi.org/10.1080/17415977.2013.830615>
- Böckmann, C., Wandinger, U., Ansmann, A., Bösenberg, J., Amiridis, V., Boselli, A., Delaval,
670 A., De Tomasi, F., Frioud, M., Grigorov, I.V., Hågård, A., Horvat, M., Iarlori, M.,
Komguem, L., Kreipl, S., Larchevêque, G., Matthias, V., Papayannis, A., Pappalardo, G.,
672 Rocadenbosch, F., Rodrigues, J.A., Schneider, J., Shcherbakov, V., Wiegner, M., 2004.
Aerosol lidar intercomparison in the framework of the EARLINET project 2 Aerosol
674 backscatter algorithms. *Appl. Opt.* 43, 977. <https://doi.org/10.1364/AO.43.000977>
- Bravo-Aranda, J.A., Navas-Guzmán, F., Guerrero-Rascado, J.L., Pérez-Ramírez, D., Granados-
676 Muñoz, M.J., Alados-Arboledas, L., 2013. Analysis of lidar depolarization calibration
procedure and application to the atmospheric aerosol characterization. *Int. J. Remote Sens.*
678 34, 3543–3560. <https://doi.org/10.1080/01431161.2012.716546>
- Bravo-Aranda, J.A., Titos, G., Granados-Muñoz, M.J., Guerrero-Rascado, J.L., Navas-Guzmán,
680 F., Valenzuela, A., Lyamani, H., Olmo, F.J., Andrey, J., Alados-Arboledas, L., 2015. Study
of mineral dust entrainment in the planetary boundary layer by lidar depolarisation
682 technique. *Tellus, Ser. B Chem. Phys. Meteorol.* <https://doi.org/10.3402/tellusb.v67.26180>
- Burton, S.P., Ferrare, R.A., Hostetler, C.A., Hair, J.W., Rogers, R.R., Obland, M.D., Butler, C.F.,
684 Cook, A.L., 2012. Aerosol classification using airborne High Spectral Resolution Lidar
measurements – methodology and examples 73–98. <https://doi.org/10.5194/amt-5-73-2012>
- 686 Burton, S.P., Hair, J.W., Kahnert, M., Ferrare, R.A., Hostetler, C.A., Cook, A.L., Harper, D.B.,
Berkoff, T.A., Seaman, S.T., Collins, J.E., Fenn, M.A., Rogers, R.R., 2015. Observations of
688 the spectral dependence of linear particle depolarization ratio of aerosols using NASA
Langley airborne High Spectral Resolution Lidar. *Atmos. Chem. Phys.* 15, 13453–13473.
690 <https://doi.org/10.5194/acp-15-13453-2015>
- Córdoba-Jabonero, C., Sorribas, M., Guerrero-Rascado, J.L., Adame, J.A., Hernández, Y.,
692 Lyamani, H., Cachorro, V., Gil, M., Alados-Arboledas, L., Cuevas, E., De La Morena, B.,
2011. Synergetic monitoring of Saharan dust plumes and potential impact on surface: A
694 case study of dust transport from Canary Islands to Iberian Peninsula. *Atmos. Chem. Phys.*
<https://doi.org/10.5194/acp-11-3067-2011>
- 696 Cwiertny, D.M., Young, M.A., Grassian, V.H., 2008. Chemistry and Photochemistry of Mineral
Dust Aerosol * . <https://doi.org/10.1146/annurev.physchem.59.032607.093630>
- 698 Denjean, C., Cassola, F., Mazzino, A., Triquet, S., Chevaillier, S., Grand, N., Bourriane, T.,
Momboisse, G., Sellegri, K., Schwarzenbock, A., Freney, E., Mallet, M., Formenti, P.,
700 2016. Size distribution and optical properties of mineral dust aerosols transported in the
western Mediterranean. *Atmos. Chem. Phys.* <https://doi.org/10.5194/acp-16-1081-2016>

- 702 Dubovik, O., Holben, B., Eck, T.F., Smirnov, A., Kaufman, Y.J., King, M.D., Tanré, D., Slutsker,
704 I., 2002. Variability of Absorption and Optical Properties of Key Aerosol Types Observed
in Worldwide Locations. *J. Atmos. Sci.* 59, 590–608. [https://doi.org/10.1175/1520-0469\(2002\)059<0590:VOAAOP>2.0.CO;2](https://doi.org/10.1175/1520-0469(2002)059<0590:VOAAOP>2.0.CO;2)
- 706 Dubovik, O., King, M.D., 2000. A flexible inversion algorithm for retrieval of aerosol optical
708 properties from Sun and sky radiance measurements. *J. Geophys. Res. Atmos.* 105, 20673–
20696. <https://doi.org/10.1029/2000JD900282>
- Dubovik, O., Sinyuk, A., Lapyonok, T., Holben, B.N., Mishchenko, M., Yang, P., Eck, T.F.,
710 Volten, H., Muñoz, O., Veihelmann, B., van der Zande, W.J., Leon, J.F., Sorokin, M.,
712 Slutsker, I., 2006. Application of spheroid models to account for aerosol particle
nonsphericity in remote sensing of desert dust. *J. Geophys. Res. Atmos.* 111, 1–34.
<https://doi.org/10.1029/2005JD006619>
- 714 Dunion, J.P., Velden, C.S., Dunion, J.P., Velden, C.S., 2004. The Impact of the Saharan Air
Layer on Atlantic Tropical Cyclone Activity. *Bull. Am. Meteorol. Soc.* 85, 353–365.
716 <https://doi.org/10.1175/BAMS-85-3-353>
- Escudero, M., Castillo, S., Querol, X., Avila, A., Alarcón, M., Viana, M.M., Alastuey, A.,
718 Cuevas, E., Rodríguez, S., 2005. Wet and dry African dust episodes over eastern Spain. *J.*
Geophys. Res. D Atmos. 110, 1–15. <https://doi.org/10.1029/2004JD004731>
- 720 Fiedler, S., Schepanski, K., Knippertz, P., Heinold, B., Tegen, I., 2014. How important are
atmospheric depressions and mobile cyclones for emitting mineral dust aerosol in North
722 Africa? *Atmos. Chem. Phys.* 14, 8983–9000. <https://doi.org/10.5194/acp-14-8983-2014>
- Flaounas, E., Kotroni, V., Lagouvardos, K., Kazadzis, S., Gkikas, A., Hatzianastassiou, N., 2015.
724 Cyclone contribution to dust transport over the Mediterranean region. *Atmos. Sci. Lett.* 16,
473–478. <https://doi.org/10.1002/asl.584>
- 726 Forster, P., V. Ramaswamy, P. Artaxo, T. Berntsen, R. Betts, D.W. Fahey, J. Haywood, J. Lean,
D.C. Lowe, G. Myhre, J. Nganga, R.P., G. Raga, M. Schulz, R.V.D., 2007. Changes in
728 Atmospheric Constituents and in Radiative Forcing, in: Solomon, S., D. Qin, M. Manning,
Z. Chen, M. Marquis, K.B. Averyt, M.T. and H.L.M. (Ed.), *Climate Change 2007: The*
730 *Physical Science Basis Contribution of Working Group I to the Fourth Assessment Report*
of the Intergovernmental Panel on Climate Change. Cambridge University Press,
732 Cambridge, United Kingdom and New York, NY, USA.
- Freudenthaler, V., 2008. The telecover test: A quality assurance tool for the optical part of a lidar
734 system. *Proc. 24th International Laser Radar Conference*, 23–27 June 2008, Boulder, CO,
USA, S01P-3.
- 736 Freudenthaler, V., Esselborn, M., Wiegner, M., Heese, B., Tesche, M., Ansmann, A., Müller, D.,
Althausen, D., Wirth, M., Fix, A., Ehret, G., Knippertz, P., Toledano, C., Gasteiger, J.,
738 Garhammer, M., Seefeldner, M., 2009a. Depolarization ratio profiling at several
wavelengths in pure Saharan dust during SAMUM 2006. *Tellus, Ser. B Chem. Phys.*
740 *Meteorol.* 61, 165–179. <https://doi.org/10.1111/j.1600-0889.2008.00396.x>
- Freudenthaler, V., Esselborn, M., Wiegner, M., Heese, B., Tesche, M., Ansmann, A., Müller, D.,
742 Althausen, D., Wirth, M., Fix, A., Ehret, G., Knippertz, P., Toledano, C., Gasteiger, J.,
Garhammer, M., Seefeldner, M., 2009b. Depolarization ratio profiling at several
744 wavelengths in pure Saharan dust during SAMUM 2006. *Tellus, Ser. B Chem. Phys.*
Meteorol. <https://doi.org/10.1111/j.1600-0889.2008.00396.x>
- 746 Freudenthaler, V., Esselborn, M., Wiegner, M., Heese, B., Tesche, M., Ansmann, A., Muller, D.,
Althausen, D., Wirth, M., Fix, A., Ehret, G., Knippertz, P., Toledano, C., Gasteiger, J.,

- 748 Garhammer, M., Seefeldner, M., 2009c. Depolarization ratio profiling at several
wavelengths in pure Saharan dust during SAMUM 2006. *Tellus B* 61, 165–179.
750 <https://doi.org/10.1111/j.1600-0889.2008.00396.x>
- Ganor, E., Osetinsky, I., Stupp, A., Alpert, P., 2010. Increasing trend of African dust, over 49
752 years, in the eastern Mediterranean. *J. Geophys. Res. Atmos.* 115, 1–7.
<https://doi.org/10.1029/2009JD012500>
- 754 Gerasopoulos, E., Amiridis, V., Kazadzis, S., Kokkalis, P., Eleftheratos, K., Andreae, M.O.,
Andreae, T.W., El-Askary, H., Zerefos, C.S., 2011. Three-year ground based measurements
756 of aerosol optical depth over the Eastern Mediterranean: The urban environment of Athens.
Atmos. Chem. Phys. 11, 2145–2159. <https://doi.org/10.5194/acp-11-2145-2011>
- 758 Giannakaki, E., Van Zyl, P.G., Müller, D., Balis, D., Komppula, M., 2016. Optical and
microphysical characterization of aerosol layers over South Africa by means of multi-
760 wavelength depolarization and Raman lidar measurements. *Atmos. Chem. Phys.* 16, 8109–
8123. <https://doi.org/10.5194/acp-16-8109-2016>
- 762 Gkikas, A., Hatzianastassiou, N., Mihalopoulos, N., 2009. Aerosol events in the broader
Mediterranean basin based on 7-year (2000–2007) MODIS C005 data. *Ann. Geophys.* 27,
764 3509–3522. <https://doi.org/10.5194/angeo-27-3509-2009>
- Gkikas, A., Houssos, E.E., Lolis, C.J., Bartzokas, A., Mihalopoulos, N., Hatzianastassiou, N.,
766 2015. Atmospheric circulation evolution related to desert-dust episodes over the
Mediterranean. *Q. J. R. Meteorol. Soc.* 141, 1634–1645. <https://doi.org/10.1002/qj.2466>
- 768 Groß S., Esselborn M., Weinzierl B., Wirth M., Fix A., and P.A., 2013. Aerosol classification by
airborne high spectral resolution lidar observations 2487–2505. <https://doi.org/10.5194/acp-13-2487-2013>
770
- Groß, S., Freudenthaler, V., Schepanski, K., Toledano, C., Schäfler, A., Ansmann, A., Weinzierl,
772 B., 2015. Optical properties of long-range transported Saharan dust over Barbados as
measured by dual-wavelength depolarization Raman lidar measurements. *Atmos. Chem.*
774 *Phys.* 15, 11067–11080. <https://doi.org/10.5194/acp-15-11067-2015>
- Groß, S., Tesche, M., Freudenthaler, V., Toledano, C., Wiegner, M., Ansmann, A., Althausen, D.,
776 Seefeldner, M., 2011a. Characterization of Saharan dust, marine aerosols and mixtures of
biomass-burning aerosols and dust by means of multi-wavelength depolarization and Raman
778 lidar measurements during SAMUM 2. *Tellus, Ser. B Chem. Phys. Meteorol.* 63, 706–724.
<https://doi.org/10.1111/j.1600-0889.2011.00556.x>
- 780 Groß, S., Tesche, M., Freudenthaler, V., Toledano, C., Wiegner, M., Ansmann, A., Althausen, D.,
Seefeldner, M., 2011b. Characterization of Saharan dust, marine aerosols and mixtures of
782 biomass-burning aerosols and dust by means of multi-wavelength depolarization and Raman
lidar measurements during SAMUM 2. *Tellus, Ser. B Chem. Phys. Meteorol.*
784 <https://doi.org/10.1111/j.1600-0889.2011.00556.x>
- Guerrero-Rascado, J.L., Costa, M.J., Bortoli, D., Silva, A.M., Lyamani, H., Alados-Arboledas, L.,
786 2010. Infrared lidar overlap function: an experimental determination. *Opt. Express* 18,
20350–9. <https://doi.org/10.1364/OE.18.020350>
- 788 Guerrero-Rascado, J.L., Olmo, F.J., Avilés-Rodríguez, I., Navas-Guzmán, F., Pérez-Ramírez, D.,
Lyamani, H., Arboledas, L.A., 2009a. Extreme saharan dust event over the southern iberian
790 peninsula in september 2007: Active and passive remote sensing from surface and satellite.
Atmos. Chem. Phys. <https://doi.org/10.5194/acp-9-8453-2009>
- 792 Guerrero-Rascado, J.L., Ruiz, B., Alados-Arboledas, L., 2008. Multi-spectral Lidar

- 794 characterization of the vertical structure of Saharan dust aerosol over southern Spain.
Atmos. Environ. 42, 2668–2681. <https://doi.org/10.1016/j.atmosenv.2007.12.062>
- Hansen, C., 2010. Discrete inverse problems: Insight and Algorithms. SIAM.
- 796 Holben, B.N., Eck, T.F., Slutsker, I., Tanré, D., Buis, J.P., Setzer, A., Vermote, E., Reagan, J.A.,
Kaufman, Y.J., Nakajima, T., Lavenu, F., Jankowiak, I., Smirnov, A., 1998. AERONET—A
798 Federated Instrument Network and Data Archive for Aerosol Characterization. Remote
Sens. Environ. 66, 1–16. [https://doi.org/10.1016/S0034-4257\(98\)00031-5](https://doi.org/10.1016/S0034-4257(98)00031-5)
- 800 Intergovernmental Panel on Climate Change (Ed.), n.d. Clouds and Aerosols, in: Climate Change
2013 - The Physical Science Basis. Cambridge University Press, Cambridge, pp. 571–658.
802 <https://doi.org/10.1017/CBO9781107415324.016>
- Kallos, G., 1998. The Regional Weather Forecasting System SKIRON and its Capability for
804 Forecasting Dust up-take and Transport. World Meteorol. Organ. TD 157–169.
- Kallos, G., Papadopoulos, A., Katsafados, P., Nickovic, S., 2006. Transatlantic Saharan dust
806 transport: Model simulation and results. J. Geophys. Res. Atmos. 111, 1–11.
<https://doi.org/10.1029/2005JD006207>
- 808 Karydis, V.A., Tsimpidi, A.P., Bacer, S., Pozzer, A., Nenes, A., Lelieveld, J., 2017. Global
impact of mineral dust on cloud droplet number concentration. Atmos. Chem. Phys 17,
810 5601–5621. <https://doi.org/10.5194/acp-17-5601-2017>
- Kim, M., Omar, A.H., Tackett, J.L., Vaughan, M.A., Winker, D.M., Trepte, C.R., Hu, Y., Liu, Z.,
812 Poole, L.R., Pitts, M.C., Kar, J., Magill, B.E., 2018. The CALIPSO version 4 automated
aerosol classification and lidar ratio selection algorithm 2, 6107–6135.
- 814 Knippertz, P., Todd, M.C., 2012. Mineral dust aerosols over the Sahara: Meteorological controls
on emission and transport and implications for modeling. Rev. Geophys. 50.
816 <https://doi.org/10.1029/2011RG000362>
- Kokkalis, P., Papayannis, A., Mamouri, R. E., Tsaknakis, G. and Amiridis, V., 2012. The EOLE
818 lidar system of the National Technical University of Athens. 26th International Laser Radar
Conference, June 25-29, 2012, Porto Heli, Greece.
- 820 Kokkalis, P., 2017. Using paraxial approximation to describe the optical setup of a typical
EARLINET lidar system. Atmos. Meas. Tech. 10, 3103–3115. <https://doi.org/10.5194/amt-10-3103-2017>
822
- Lopatin, A., Dubovik, O., Chaikovsky, A., Goloub, P., Lapyonok, T., Tanre´, D., Litvinov, P.,
824 2013. Enhancement of aerosol characterization using synergy of lidar and sun-photometer
coincident observations : the GARRLiC algorithm 2065–2088. <https://doi.org/10.5194/amt-6-2065-2013>
826
- Lyamani, H., Olmo, F.J., Alados-Arboledas, L., 2010. Physical and optical properties of aerosols
828 over an urban location in Spain: Seasonal and diurnal variability. Atmos. Chem. Phys. 10,
239–254. <https://doi.org/10.5194/acp-10-239-2010>
- 830 Lyamani, H., Olmo, F.J., Alados-Arboledas, L., 2008. Light scattering and absorption properties
of aerosol particles in the urban environment of Granada, Spain. Atmos. Environ. 42, 2630–
832 2642. <https://doi.org/10.1016/j.atmosenv.2007.10.070>
- Lyamani, H., Olmo, F.J., Alados-Arboledas, L., 2005. Saharan dust outbreak over southeastern
834 Spain as detected by sun photometer. Atmos. Environ. 39, 7276–7284.
<https://doi.org/10.1016/j.atmosenv.2005.09.011>
- 836 Lyamani, H., Olmo, F.J., Alcántara, A., Alados-Arboledas, L., 2006a. Atmospheric aerosols

- 838 during the 2003 heat wave in southeastern Spain I: Spectral optical depth. *Atmos. Environ.*
40, 6453–6464. <https://doi.org/10.1016/j.atmosenv.2006.04.048>
- 840 Lyamani, H., Olmo, F.J., Alcántara, A., Alados-Arboledas, L., 2006b. Atmospheric aerosols
during the 2003 heat wave in southeastern Spain II: Microphysical columnar properties and
842 radiative forcing. *Atmos. Environ.* 40, 6465–6476.
<https://doi.org/10.1016/j.atmosenv.2006.04.047>
- 844 Mamouri, R.E., Ansmann, A., 2015. Estimated desert-dust ice nuclei profiles from polarization
lidar: Methodology and case studies. *Atmos. Chem. Phys.* 15, 3463–3477.
<https://doi.org/10.5194/acp-15-3463-2015>
- 846 Matthais, V., Freudenthaler, V., Amodeo, A., Balin, I., Balis, D., Bösenberg, J., Chaikovskiy, A.,
Chourdakis, G., Comeron, A., Delaval, A., De Tomasi, F., Eixmann, R., Hågård, A.,
848 Komguem, L., Kreipl, S., Matthey, R., Rizi, V., Rodrigues, J.A., Wandinger, U., Wang, X.,
2004. Aerosol lidar intercomparison in the framework of the EARLINET project. 1.
850 *Instruments. Appl. Opt.* 43, 961–76.
- 852 Mattis, I., Ansmann, A., Müller, D., Wandinger, U., Althausen, D., 2002a. Dual-wavelength
Raman lidar observations of the extinction-to-backscatter ratio of Saharan dust. *Geophys.*
Res. Lett. 29, 20–21. <https://doi.org/10.1029/2002GL014721>
- 854 Mattis, I., Ansmann, A., Müller, D., Wandinger, U., Althausen, D., 2002b. Dual-wavelength
Raman lidar observations of the extinction-to-backscatter ratio of Saharan dust. *Geophys.*
856 *Res. Lett.* <https://doi.org/10.1029/2002gl014721>
- 858 Mattis, I., Müller, D., Ansmann, A., Wandinger, U., Preißler, J., Seifert, P., Tesche, M., 2008.
Ten years of multiwavelength Raman lidar observations of free-tropospheric aerosol layers
over central Europe: Geometrical properties and annual cycle. *J. Geophys. Res. Atmos.* 113.
860 <https://doi.org/10.1029/2007JD009636>
- 862 Mona, L., Amodeo, A., Pandolfi, M., Pappalardo, G., 2006. Saharan dust intrusions in the
Mediterranean area: Three years of Raman lidar measurements. *J. Geophys. Res. Atmos.*
111, 1–13. <https://doi.org/10.1029/2005JD006569>
- 864 Mona, L., Liu, Z., Müller, D., Omar, A., Papayannis, A., Pappalardo, G., Sugimoto, N., Vaughan,
M., 2012. Lidar measurements for desert dust characterization: An overview. *Adv.*
866 *Meteorol.* 2012. <https://doi.org/10.1155/2012/356265>
- 868 Müller, D., Ansmann, A., Mattis, I., Tesche, M., Wandinger, U., Althausen, D., Pisani, G., 2007.
Aerosol-type-dependent lidar ratios observed with Raman lidar. *J. Geophys. Res. Atmos.*
112. <https://doi.org/10.1029/2006JD008292>
- 870 Müller, D., Böckmann, C., Kolgotin, A., Schneidenbach, L., Chemyakin, E., Rosemann, J., Znak,
P., Romanov, A., 2016. Microphysical particle properties derived from inversion algorithms
872 developed in the framework of EARLINET. *Atmos. Meas. Tech* 9, 5007–5035.
<https://doi.org/10.5194/amt-9-5007-2016>
- 874 Müller, D., Heinold, B., Tesche, M., Tegen, I., Althausen, D., Arboledas, L.A., Amiridis, V.,
Amodeo, A., Ansmann, A., Balis, D., Comeron, A., D’amico, G., Gerasopoulos, E.,
876 Guerrero-rascado, J.L., Freudenthaler, V., Giannakaki, E., Heese, B., Iarlori, M., Knippertz,
P., Mamouri, R.E., Mona, L., Papayannis, A., Pappalardo, G., Perrone, R.M., Pisani, G.,
878 Rizi, V., Sicard, M., Spinelli, N., Tafuro, A., Wiegner, M., 2009. EARLINET observations
of the 14-22-May long-range dust transport event during SAMUM 2006: Validation of
880 results from dust transport modelling. *Tellus, Ser. B Chem. Phys. Meteorol.* 61, 325–339.
<https://doi.org/10.1111/j.1600-0889.2008.00400.x>

- 882 Navas-Guzmán, F., Rascado, J.L.G., Arboledas, L.A., 2011. Retrieval of the lidar overlap
function using Raman signals. *Opt. Pura Apl* 44, 71–75.
- 884 Nicolae, D., Nemuc, A., Müller, D., Talianu, C., Vasilescu, J., Belegante, L., Kolgotin, A., 2013.
886 Characterization of fresh and aged biomass burning events using multiwavelength Raman
lidar and mass spectrometry. *J. Geophys. Res. Atmos.* 118, 2956–2965.
<https://doi.org/10.1002/jgrd.50324>
- 888 Papayannis, A., Amiridis, V., Mona, L., Tsaknakis, G., Balis, D., Bösenberg, J., Chaikovski, A.,
Tomasi, F. De, Grigorov, I., Mattis, I., Mitev, V., Müller, D., Nickovic, S., Pérez, C.,
890 Pietruczuk, A., Pisani, G., Ravetta, F., Rizi, V., Sicard, M., Trickl, T., Wiegner, M.,
Gerding, M., Mamouri, R.E., D’Amico, G., Pappalardo, G., 2008. Systematic lidar
892 observations of Saharan dust over Europe in the frame of EARLINET (2000–2002). *J.*
Geophys. Res. Atmos. 113. <https://doi.org/10.1029/2007JD009028>
- 894 Papayannis, A., Ancellet, G., Pelon, J., Mégie, G., 1990. Multiwavelength lidar for ozone
measurements in the troposphere and the lower stratosphere. *Appl. Opt.* 29, 467–76.
896 <https://doi.org/10.1364/AO.29.000467r60866>
- Papayannis, A., Balis, D., Amiridis, V., Chourdakis, G., Tsaknakis, G., Zerefos, C., Castanho,
898 A.D.A., Nickovic, S., Kazadzis, S., Grabowski, J., 2005. Measurements of Saharan dust
aerosols over the Eastern Mediterranean using elastic backscatter-Raman lidar,
900 spectrophotometric and satellite observations in the frame of the EARLINET project.
Atmos. Chem. Phys 5, 2065–2079.
- 902 Pappalardo, G., Amodeo, A., Apituley, A., Comeron, A., Freudenthaler, V., Linné, H., Ansmann,
A., Bösenberg, J., D’amico, G., Mattis, I., Mona, L., Wandinger, U., Amiridis, V., Alados-
904 Arboledas, L., Nicolae, D., Wiegner, M., 2014. EARLINET: towards an advanced
sustainable European aerosol lidar network. *Atmos. Meas. Tech* 7, 2389–2409.
906 <https://doi.org/10.5194/amt-7-2389-2014>
- Pérez, C., Nickovic, S., Baldasano, J.M., Sicard, M., Rocadenbosch, F., Cachorro, V.E., 2006. A
908 long Saharan dust event over the western Mediterranean: Lidar, Sun photometer
observations, and regional dust modeling. *J. Geophys. Res. Atmos.* 111, 1–16.
910 <https://doi.org/10.1029/2005JD006579>
- Petzold, A., Rasp, K., Weinzierl, B., Esselborn, M., Hamburger, T., Dörnbrack, A., Kandler, K.,
912 Schütz, L., Knippertz, P., Fiebig, M., Virkkula, A., 2009. Saharan dust absorption and
refractive index from aircraft-based observations during SAMUM 2006. *Tellus, Ser. B*
914 *Chem. Phys. Meteorol.* 61, 118–130. <https://doi.org/10.1111/j.1600-0889.2008.00383.x>
- Preißler, J., Wagner, F., Guerrero-Rascado, J.L., Silva, A.M., 2013. Two years of free-
916 tropospheric aerosol layers observed over Portugal by lidar. *J. Geophys. Res. Atmos.* 118,
3676–3686. <https://doi.org/10.1002/jgrd.503502013>
- 918 Preißler, J., Wagner, F., Pereira, S.N., Guerrero-Rascado, J.L., 2011. Multi-instrumental
observation of an exceptionally strong Saharan dust outbreak over Portugal. *J. Geophys.*
920 *Res. Atmos.* <https://doi.org/10.1029/2011JD016527>
- Prospero, J.M., 1996. Saharan dust transport over the North Atlantic Ocean and the
922 Mediterranean, in *The Impact of Desert Dust Across the Mediterranean*. Springer, New
York.
- 924 Prospero, J.M., Ginoux, P., Torres, O., Nicholson, S.E., Gill, T.E., 2002. Environmental
characterization of global sources of atmospheric soil dust identified with the nimbus 7 total
926 ozone mapping spectrometer (TOMS) absorbing aerosol product. *Rev. Geophys.* 40, 1–2.
<https://doi.org/10.1029/2000RG000095>

- 928 Rolph, G., Stein, A., Stunder, B., 2017. Real-time Environmental Applications and Display
 sYstem: READY. *Environ. Model. Softw.* 95, 210–228.
 930 <https://doi.org/10.1016/j.envsoft.2017.06.025>
- Rother, T., Kahnert, M., 2009. Electromagnetic Wave Scattering on Nonspherical Particles.
 932 <https://doi.org/10.1007/978-3-642-00704-0>
- Salvador, P., Alonso-Pérez, S., Pey, J., Artíñano, B., De Bustos, J.J., Alastuey, A., Querol, X.,
 934 2014. African dust outbreaks over the western Mediterranean Basin: 11-year
 characterization of atmospheric circulation patterns and dust source areas. *Atmos. Chem.*
 936 *Phys.* 14, 6759–6775. <https://doi.org/10.5194/acp-14-6759-2014>
- Samaras, S., 2016. Microphysical retrieval of non-spherical aerosol particles using regularized
 938 inversion of multi-wavelength lidar data. PhD Thesis. Institut für Mathematik, Numerische
 Mathematik - Inverse Probleme, University of Potsdam, Germany.
- 940 Samaras, S., Nicolae, D., Böckmann, C., Vasilescu, J., Biniotoglou, I., Labzovskii, L., Toanca, F.,
 Papayannis, A., 2015. Using Raman-lidar-based regularized microphysical retrievals and
 942 Aerosol Mass Spectrometer measurements for the characterization of biomass burning
 aerosols. *J. Comput. Phys.* 299, 156–174. <https://doi.org/10.1016/j.jcp.2015.06.045>
- 944 Sassen, K., 2005. Polarization in Lidar, in: C., W. (Ed.), *Lidar Range-Resolved Optical Remote
 Sensing of the Atmosphere*. Springer, pp. 19–42. <https://doi.org/10.1007/978-1-4612-3262-9>
- 946 Schepanski, K., Knippertz, P., 2011. Soudano-Saharan depressions and their importance for
 precipitation and dust: A new perspective on a classical synoptic concept. *Q. J. R. Meteorol.*
 948 *Soc.* 137, 1431–1445. <https://doi.org/10.1002/qj.850>
- Schladitz, A., Muller, T., Kaaden, N., Massling, A., Kandler, K., Ebert, M., Weinbruch, S.,
 950 Deutscher, C., Wiedensohler, A., 2009. In situ measurements of optical properties at Tinfou
 (Morocco) during the Saharan Mineral Dust Experiment SAMUM 2006 64–78.
 952 <https://doi.org/10.1111/j.1600-0889.2008.00397.x>
- Schuster, G.L., Dubovik, O., Arola, A., 2016. Remote sensing of soot carbon – Part 1 :
 954 Distinguishing different absorbing aerosol species 1565–1585. <https://doi.org/10.5194/acp-16-1565-2016>
- 956 Seinfeld, J.H., Bretherton, C., Carslaw, K.S., Coe, H., DeMott, P.J., Dunlea, E.J., Feingold, G.,
 Ghan, S., Guenther, A.B., Kahn, R., Kraucunas, I., Kreidenweis, S.M., Molina, M.J., Nenes,
 958 A., Penner, J.E., Prather, K.A., Ramanathan, V., Ramaswamy, V., Rasch, P.J.,
 Ravishankara, A.R., Rosenfeld, D., Stephens, G., Wood, R., 2016. Improving our
 960 fundamental understanding of the role of aerosol–cloud interactions in the climate system.
Proc. Natl. Acad. Sci. 113, 5781–5790. <https://doi.org/10.1073/pnas.1514043113>
- 962 Soupiona, O., Papayannis, A., Kokkalis, P., Mylonaki, M., Tsaknakis, G., Argyrouli, A., Vratolis,
 S., 2018. Long-term systematic profiling of dust aerosol optical properties using the EOLE
 964 NTUA lidar system over Athens, Greece (2000–2016). *Atmos. Environ.* 183, 165–174.
<https://doi.org/10.1016/j.atmosenv.2018.04.011>
- 966 Stein, A.F., Draxler, R.R., Rolph, G.D., Stunder, B.J.B., Cohen, M.D., Ngan, F., 2015. Noaa’s
 hysplit atmospheric transport and dispersion modeling system. *Bull. Am. Meteorol. Soc.* 96,
 968 2059–2077. <https://doi.org/10.1175/BAMS-D-14-00110.1>
- Tesche, M., Gross, S., Ansmann, A., Müller, D., Althausen, D., Freudenthaler, V., Esselborn, M.,
 970 2011. Profiling of Saharan dust and biomass-burning smoke with multiwavelength
 polarization Raman lidar at Cape Verde. *Tellus B Chem. Phys. Meteorol.* 63, 649–676.
 972 <https://doi.org/10.1111/j.1600-0889.2011.00548.x>

974 Toledano, C., Wiegner, M., Groß, S., Freudenthaler, V., Gasteiger, J., Müller, D., Schladitz, A.,
 976 Weinzierl, B., Torres, B., O'Neill, N.T., Wiegner, M., Groß, S., Freudenthaler, V., Gasteiger, J.,
 978 Müller, D., Müller, D., Schladitz, A., Weinzierl, B., Torres, B., O'Neill, N.T., 2011. Optical
 980 properties of aerosol mixtures derived from sun-sky radiometry during SAMUM-2. *Tellus B*
 982 63B, 635–648. <https://doi.org/10.1111/j.1600-0889.2011.00573.x>

984 Valenzuela A., Olmo F. J., Lyamani H., Granados-Muñoz M. J., Antón M., Guerrero-Rascado J.
 986 L., Quirantes A., Toledano C., Perez-Ramirez D., A.A.L., 2014. Aerosol transport over the
 988 western Mediterranean basin: Evidence of the contribution of fine particles to desert dust
 990 plumes over Alborán Island. *J. Geophys. Atmos.* 119, 14,028–14,044.
 992 <https://doi.org/doi:10.1002/2014JD022044>

994 Valenzuela, A., Olmo, F.J., Lyamani, H., Antón, M., Quirantes, A., Alados-Arboledas, L., 2012.
 996 Analysis of the columnar radiative properties retrieved during African desert dust events
 over Granada (2005-2010) using principal plane sky radiances and spheroids retrieval
 procedure. *Atmos. Res.* 104–105, 292–301. <https://doi.org/10.1016/j.atmosres.2011.11.005>

998 Valenzuela, A., Olmo, F.J., Lyamani, H., Granados-Muñoz, M.J., Antón, M., Guerrero-Rascado,
 1000 J.L., Quirantes, A., Toledano, C., Perez-Ramírez, D., Alados-Arboledas, L., 2014. Aerosol
 1002 transport over the western mediterranean basin: Evidence of the contribution of fine
 1004 particles to desert dust plumes over alborán island. *J. Geophys. Res.*
 1006 <https://doi.org/10.1002/2014JD022044>

1008 Veselovskii, I., Goloub, P., Podvin, T., Bovchaliuk, V., Derimian, Y., Augustin, P., Fourmentin,
 1010 M., Tanre, D., Korenskiy, M., Whiteman, D.N., Diallo, A., Ndiaye, T., Kolgotin, A.,
 1012 Dubovik, O., 2016. Retrieval of optical and physical properties of African dust from
 1014 multiwavelength Raman lidar measurements during the SHADOW campaign in Senegal.
 1016 *Atmos. Chem. Phys* 16, 7013–7028. <https://doi.org/10.5194/acp-16-7013-2016>

1018 Wagner, R., Ajtai, T., Kandler, K., Lieke, K., Linke, C., Muller, T., Schnaiter, M., Vragel, M.,
 1020 2012. and Physics Complex refractive indices of Saharan dust samples at visible and near
 1022 UV wavelengths : a laboratory study 2491–2512. <https://doi.org/10.5194/acp-12-2491-2012>

1024 Wandinger, U., Baars, H., Engelmann, R., Hünerbein, A., Horn, S., Kanitz, T., Donovan, D., van
 1026 Zadelhoff, G.-J., Daou, D., Fischer, J., von Bismarck, J., Filipitsch, F., Docter, N., Eisinger,
 1028 M., Lajas, D., Wehr, T., 2016. HETEAC: The Aerosol Classification Model for
 1030 EarthCARE. *EPJ Web Conf.* 119, 01004. <https://doi.org/10.1051/epjconf/201611901004>

1032 Washington, R., Todd, M., Middleton, N.J., Goudie, A.S., 2003. Dust-storm source areas
 1034 determined by the total ozone monitoring spectrometer and surface observations. *Ann.*
 1036 *Assoc. Am. Geogr.* 93, 297–313. <https://doi.org/10.1111/1467-8306.9302003>

1038 Weinzierl, B., Sauer, D., Esselborn, M., Petzold, A., Veira, A., Rose, M., Mund, S., Wirth, M.,
 1040 Ansmann, A., Tesche, M., Gross, S., Freudenthaler, V., 2011. Microphysical and optical
 1042 properties of dust and tropical biomass burning aerosol layers in the Cape Verde region-an
 1044 overview of the airborne in situ and lidar measurements during SAMUM-2. *Tellus, Ser. B*
 1046 *Chem. Phys. Meteorol.* <https://doi.org/10.1111/j.1600-0889.2011.00566.x>

1048 Zuev, V. V., Burlakov, V.D., Nevzorov, A. V., Pravdin, V.L., Savelieva, E.S., Gerasimov, V. V.,
 1050 2017. 30-year lidar observations of the stratospheric aerosol layer state over Tomsk
 1052 (Western Siberia, Russia). *Atmos. Chem. Phys* 17, 3067–3081. <https://doi.org/10.5194/acp-17-3067-2017>